Constrained Multi-Body Dynamics for Modular Underwater Robots — Theory and Experiments

Mikkel Cornelius Nielsen[a,c], Ole Alexander Eidsvik[b], Mogens Blanke[a,c], Ingrid Schjølberg[b]

[a] *Center for Autonomous Marine Operations and Systems, Department of Engineering Cybernetics, Norwegian University of Science and Technology, Trondheim, Norway*

[b] *Center for Autonomous Marine Operations and Systems, Department of Marine Technology, Norwegian University of Science and Technology, Trondheim, Norway*

[c] *Department of Electrical Engineering, Automation and Control Group, Technical University of Denmark, Lyngby, Denmark*

Abstract

This paper investigates the problem of modelling a system of interconnected underwater robots with highly coupled dynamics. The objective is to develop a mathematical description of the system that captures its most significant dynamics. The proposed modelling method is based on active constraint enforcement by utilising the Udwadia-Kalaba Formulation for multi-body dynamics. The required description of a rigid constraint is defined, derived and implemented into a system of interconnected sub-models. An exhaustive experimental validation is conducted on a two-vehicle system, including towing tank tests on a BlueROV vehicle to determine the model parameters. The applicability of the modelling approach is assessed by comparing experimental data to simulations of an equivalent model synthesised using the proposed theory.

Keywords:
Multi-body Dynamics, Udwadia-Kalaba Equation, Modular Underwater Robots, Constrained Dynamics, Quasi-Coordinates, Re-configurable Robots

1. Introduction

Autonomy in the offshore sector is projected to increase rapidly as a result of attempts to reduce cost, increase safety and production in a progressively hostile environment. The future of sub-sea facilities are in deeper, colder and more remote locations. These sub-sea facilities are exposed to the harsh conditions in the open ocean that offers no shelter. Damages induced under such harsh conditions are inevitable and development of safe and reliable *Inspection, Maintenance and Repair* (IMR) equipment is an unparalleled necessity Schjølberg et al. (2016); Sanz et al. (2010).

IMR operations are currently conducted by *Remotely Operated Vehicles* (ROVs) operated by a team of pilots. The type of ROV used in IMR operations are most commonly the *working-class* ROV, which entails a multiple ton vehicle with an array of utility and a powerful propulsion system to overcome the effects of both the umbilical cable and the manipulation task. A common configuration for controlling working-class ROVs is one pilot to navigate the vehicle itself, while a co-pilot controls the manipulation and intervention itself. The size of the working-class ROV is a limiting factor, which restricts the operations to the exterior of the structures. Damages discovered by small *observation-class* ROVs may not be reachable by the appropriate sized intervention type ROV.

To overcome such a limitation it is envisioned that IMR operations could be conducted by groups of small sized cooperating ROVs or *Intervention Autonomous Underwater Vehicles* (I-AUVs) with intervention capabilities. Intervention capable AUVs is an active field of research and multiple authors have considered the modelling and control of I-AUVs Allotta et al. (2013), Palomeras et al. (2016), Moe et al. (2014), Casalino et al. (2014). Conti et al. (2015) presented a state-of-the-art method for using multiple I-AUVs in a coooperative manipulation task based on

a potential-field approach. A cooperative system with persistent presence would allow for more reliable real-time feedback of the current conditions of the platform. Compared to the monolithic working-class vehicle each individual vehicle within the cooperative group could be outfitted with different payloads and thereby allow for more flexible and fault-tolerant operations at a lower cost.

A particularly relevant utilization of such as system would be the transportation of tools in confined sub-sea environments. In such a scenario multiple smaller vehicle could cooperatively work together in manoeuvring an intervention tool to areas otherwise inaccessible. Manoeuvring and control of cooperative systems will require insight into the interaction between the vehicles during motion and kinematic and dynamic modelling is necessary for any meaningful investigation on how to control such a system.

Modelling of marine systems has been researched extensively in the past. Parametric identification through towing tank tests are prohibitively expensive and preliminary analysis of any given design is often carried out using *Computational-Fluid-Dynamics* (CFD). CFD analysis can also be used post design using *Virtual Captive Test* (VCT) as was presented in Ramírez-Macías et al. (2016). System identification through usage of CFD, however, is not always reliable and experimental data is highly valued when available.

One approach to system identification is through the classical system identification methodology of input to output behaviour. These system identification techniques has been applied in various different scenarios such as Caccia et al. (2000); Pereira and Duncan (2000); Kim et al. (2002); Ridao et al. (2004); Marco et al. (1998); Valeriano-Medina et al. (2012) and Ferri et al. (2013). Common for all the methods is that the capture of motion data often requires a lot of both space and time.

Another approach is to apply specific known force externally to the system and measure the reaction. Ross et al. (2004) presented free decay tests as a method for identifying parameters for underwater vehicles using spring forces as excitation. A similar approach was presented in Eng et al. (2008) using pendulum motion to identify ROV parameters.

Motion based approaches to identify parameters most often lump parameters together to yield a cruder model. When available, towing tank tests using a Planar-Motion-Mechanism (PMM) is the preferred standard for modelling, as it allows modelling of the dynamics of all axes. Parameters of a ROV were identified using PMM tests in Avila and Adamowski (2011) and Avila et al. (2012). Recently, Eidsvik and Schjølberg (2016a) tested a new approximating modelling strategy against PMM tests with promising results.

Single vehicle models, such as the models in Fossen (2011), works particularly well for AUVs and surface vessels, however, the dynamics of a ROV is often dominated by the dynamics of the cable attaching it to the surface. Modelling of cables has been approached in different ways.

A series of papers Huston and Kamman (1982); Kamman and Huston (1985, 2001) modelled underwater cables using multi-body dynamics instead of using Finite-Element-Methods. Park and Kim (2015) modelled a system consisting of a semi-submersible vehicle towing a tow-fish by a cable using multi-body dynamics with a lumped-mass approximation. Gomes et al. (2016) modelled underwater cables using a finite chain of rigid-bodies connected using flexible joints and Eidsvik and Schjølberg (2016b) used beam equations to model the umbilical cable of a ROV.

New applications such as intervention missions have introduced new devices, including manipulator arms for interaction. Modeling and control of I-AUVs and *Underwater Vehicle-Manipulator System* (UVMS) have received attention in the field. Traditional approach to modelling of manipulator arms are by utilization of multi-body dynamics and for sub-sea application the multi-body perspective has also been applied successfully.

Tarn et al. (1996) applied Kane's method to model a Robotic Manipulator mounted on an Underwater Vehicle. Yang (2016) presented a modelling method based on graph-theoretical tools to generate a dynamic model for re-configurable underwater robots using Kane's method. Santhakumar (2013) modelled an UVMS using a closed-form multi-body dynamics approach. Huang et al. (2016) derived another UVMS model using a Newton-Eulerian formalism of dynamics instead of the classical Lagrangian Formulation often seen in manipulator derivation. A general overview of UVMS modelling and control was presented in Antonelli (2014).

With the advent of Biomimetics in underwater environments, recent articles have employed multi-body dynamics to model their systems. Krishnamurthy et al. (2009) introduced a general 6-DOF multi-body framework for modelling

biomimetic underwater vehicles and demonstrated it using a ray-fish as application. Kelasidi et al. (2014b), Kelasidi et al. (2014a) and Kelasidi et al. (2015) used multi-body dynamics to synthesize and validate an amphibious underwater snake model.

This article extends and validates the multi-body dynamic modelling approach in Nielsen et al. (2016a) and Nielsen et al. (2016b), which using the Udwadia-Kalaba formulation Udwadia and Phohomsiri (2007). This article first presents the theoretical approach used to model a system of re-configurable underwater robots. As a first step, the paper develops the constraints necessary to rigidly connect the robots and then shows how the Udwadia-Kalaba formulation for multi-body dynamics is conveniently employed to obtain a dynamic model of an arbitrary configuration of modular robots. The article then presents experimental validations of the theoretical model. The validation use time-series comparisons between a range of motion patterns performed by a real system and an equivalent set of simulations. Finally, the hydrodynamic parameters of a BlueROV underwater vehicle is obtained as a by-product of the experimental validation.

The organization of the article is as follows. The theoretical background for the solution is presented in Section 2 along with derivation of relevant constraints. Section 3 then details on the experimental validation setup for both single vehicle and multi-vehicle experiments. Results of the experimental data are analyzed and discussed in Section 4 and Section 6 holds the conclusions.

2. Theory

This section first introduces the notation used in the rest of the paper. Thereafter, the model for the single vehicle system is presented in Section. 2.2. In Section 2.3 the theoretical multi-body model based on the Udwadia-Kalaba Formulation is given.

2.1. Kinematics

The notation adopted in this paper is the SNAME as presented in Fossen (2011) and used in Nielsen et al. (2016a).

Two reference frames are introduced, a global fixed frame to relate the pose of the individual models and a moving local frame attached to each rigid body of the system. The global frame is a flat-earth approximation frame assumed to be inertial and denoted by $\{n\}$ while the local body-fixed reference frame is denoted by $\{b\}$. A pose in the global frame is denoted $\boldsymbol{\eta}$ and consists of a position $\boldsymbol{p}^n_{b/n} \in \mathbb{R}^3$ and the orientation of the local frame relative to the global frame $\boldsymbol{q} \in \mathbb{R}^4$. The orientation is parametrised by a unit quaternion to avoid singularities in the description. The unit quaternion $\boldsymbol{q}$ is expressed using by one real part η and three imaginary parts ε_i $i \in \{1, 2, 3\}$ such that $\boldsymbol{q} = [\eta, \varepsilon_1, \varepsilon_2, \varepsilon_3]^T$. The body-fixed velocities are denoted $\boldsymbol{\nu}$ and defined as follows

$$\boldsymbol{\nu}^b_{b/n} = [u,\ v,\ w,\ p,\ q,\ r]^T \in \mathbb{R}^6 \tag{1}$$

As was the case of the pose vector, the body-fixed velocities can also be separated into linear and rotational sub-parts, where $\boldsymbol{\nu}^b_{b/n} = [u, v, w]^T$ represents the linear velocities and $\boldsymbol{\omega}^b_{b/n} = [p, q, r]^T$ represents the angular velocities. The transformation of linear velocity in body-fixed to the navigation frame is conducted through the rotation matrix below

$$\boldsymbol{R}^n_b = \begin{bmatrix} 1 - 2\left(\varepsilon_2^2 + \varepsilon_3^2\right) & 2\left(\varepsilon_1\varepsilon_2 - \varepsilon_3\eta\right) & 2\left(\varepsilon_1\varepsilon_3 + \varepsilon_2\eta\right) \\ 2\left(\varepsilon_1\varepsilon_2 + \varepsilon_3\eta\right) & 1 - 2\left(\varepsilon_1^2 + \varepsilon_3^2\right) & 2\left(\varepsilon_2\varepsilon_3 - \varepsilon_1\eta\right) \\ 2\left(\varepsilon_1\varepsilon_3 - \varepsilon_2\eta\right) & 2\left(\varepsilon_2\varepsilon_3 + \varepsilon_1\eta\right) & 1 - 2\left(\varepsilon_1^2 + \varepsilon_2^2\right) \end{bmatrix} \tag{2}$$

The attitude change $\boldsymbol{\omega}^b_{b/n}$ is related to the change of the relative orientation between local and global frame through the transformation matrix $\boldsymbol{T}_q$ defined below

$$\dot{\boldsymbol{q}} = \boldsymbol{T}_q \boldsymbol{\omega}^b_{b/n} \tag{3}$$

where the transformation matrix $\boldsymbol{T}_q$ is defined as

$$\boldsymbol{T}_q = \frac{1}{2}\boldsymbol{H}^T = \frac{1}{2}\begin{bmatrix} -\varepsilon_1 & -\varepsilon_2 & -\varepsilon_3 \\ \eta & -\varepsilon_3 & \varepsilon_2 \\ \varepsilon_3 & \eta & -\varepsilon_1 \\ -\varepsilon_2 & \varepsilon_1 & \eta \end{bmatrix} \tag{4}$$

such that $\boldsymbol{H}$ is

$$\boldsymbol{H} = [-\boldsymbol{\varepsilon},\ \eta\boldsymbol{I}_3 - \boldsymbol{S}(\boldsymbol{\varepsilon})] \in \mathbb{R}^{3\times 4} \tag{5}$$

The skew-symmetric matrix $\boldsymbol{S}(\boldsymbol{\lambda})$ represents the a cross product operation such that

$$\boldsymbol{\lambda}\times = \boldsymbol{S}(\boldsymbol{\lambda}) = \begin{bmatrix} 0 & -\lambda_3 & \lambda_2 \\ \lambda_3 & 0 & -\lambda_1 \\ -\lambda_2 & \lambda_1 & 0 \end{bmatrix}$$

The translational and rotational transformations can be aggregated into combined matrix form as follows

$$\boldsymbol{J}_q = \begin{bmatrix} \boldsymbol{R}_b^n & \boldsymbol{0}_{3\times 3} \\ \boldsymbol{0}_{4\times 3} & \boldsymbol{T}_q \end{bmatrix} \tag{6}$$

The kinetics of a single vehicle is affected as follows.
Assumption 2.1. *The fluid is viscid and incompressible.*
Remark 2.1. *Assumption 2.1 is common in hydrodynamic modelling.*

2.2. Single Vehicle Dynamics

The dynamics of the individual sub-model is required to synthesis the global model. A sub-model in the system is described by Fossens Robot-like model shown below.

$$\boldsymbol{M}\dot{\boldsymbol{\nu}} + \boldsymbol{D}(\boldsymbol{\nu})\boldsymbol{\nu} + \boldsymbol{C}(\boldsymbol{\nu})\boldsymbol{\nu} + \boldsymbol{g}(\boldsymbol{\eta}) = \boldsymbol{\tau} \tag{7}$$

where $\boldsymbol{M}$ is the inertia matrix containing both rigid-body inertia and hydrodynamic added mass, $\boldsymbol{D}$ is the hydrodynamic damping, $\boldsymbol{C}$ is a matrix with Coriolis terms, $\boldsymbol{g}$ is the gravity vector and $\boldsymbol{\tau}$ is the applied force. The model in Eq. (7) form basis for the local model of the combined system, it is easily extended to relative velocities taking into account currents. In general the inertia matrix $\boldsymbol{M}$ and damping matrix $\boldsymbol{D}$ will be dense matrices leading to coupled motions between each *degree of freedom* (DOF), however, identification of off-diagonal parameters is very difficult. Therefore an assumption of uncoupled motion is made as follows
Assumption 2.2. *The axes of the body-fixed coordinate frame is aligned with the principle axes of the vehicle and the principle axes are aligned with the axes of symmetry. Hence the off-diagonal elements of $\boldsymbol{M}$ and $\boldsymbol{D}$ are zero and the motion of each degree of freedom is uncoupled.*
Remark 2.2. *Assumption 2.2 is valid if the ROV has three planes of symmetry and move at low speed, which is a common assumption in many ROV and AUV applications. See (Fossen, 2011, p. 121).*

The actuation input for the vehicle $\boldsymbol{\tau}$ is a result of the combination of thrusters mounted on the vehicle. Thrusters are located on the vehicle relative to the centre of origin (CO). Each thruster contains a local frame aligned with the direction of thrust produced. The thrust exerted in the body-frame of the vehicle is then calculated by transforming the thrust from the thruster-frame to the body-frame. Since the local x-axis is parallel with the produced thrust direction any rotation around said x-axis will not change the thrust generated in the vehicles body-frame. Instead the

transformation from the local thruster to the body frame can be written as follows

$$\begin{aligned}\boldsymbol{\tau}^b_{j/b} &= \boldsymbol{t}^b_j \tau_j \\ &= \begin{bmatrix} \cos(\alpha_j)\cos(\beta_j) \\ -\cos(\alpha_j)\sin(\beta_j) \\ \sin(\alpha_j) \end{bmatrix} \tau_j \end{aligned} \tag{8}$$

where subscript j denotes the jth thruster such that α_j and β_j are angles relating the direction of thruster j with respect to the body-fixed frame of the vehicle. The actuation $\boldsymbol{\tau}$ is the result of the combined thrust from each thruster.

$$\boldsymbol{\tau} = \sum_{j \in \mathcal{J}} \boldsymbol{h}\left(\boldsymbol{\tau}^b_{j/b}, \boldsymbol{p}^b_{j/b}\right) = \sum_{j \in \mathcal{J}} \begin{bmatrix} \boldsymbol{\tau}^b_{j/b} \\ \boldsymbol{p}^b_{j/b} \times \boldsymbol{\tau}^b_{j/b} \end{bmatrix} \tag{9}$$

where $\mathcal{J}$ is the set of thrusters mounted on the robot and $\boldsymbol{p}^b_{j/b}$ is the body-fixed position of thruster j. The force generated by the thruster τ_j depends on the motor driving the propeller and the propeller itself. Commonly propellers

Table 1: Nomenclature for single vehicle Dynamics

Symbol	Name	Unit
u_a	Advance Speed	$\left(\frac{m}{s}\right)$
ω	Propeller shaft speed	$\left(\frac{rad}{s}\right)$
J	Advance Ratio	$(-)$
K_T	Thrust Coefficient	$(-)$
ρ	Water Density	$\left(\frac{kg}{m^3}\right)$
D	Propeller Diameter	(m)
$T_{\lvert\omega\rvert\omega}$	Thrust Coefficient	(kgm)
$T_{\lvert\omega\rvert u}$	Thrust Coefficient	(kg)
τ_p	Propeller Thrust	(N)

are modelled in non-dimensional form and as such they can be described by the non-dimensional coefficient K_T defined below

$$K_T = \tau_p \frac{4\pi^2}{\rho|\omega|\omega D^4} \tag{10}$$

where τ_p is the thrust output of the propeller, ρ is the density of the water, ω is the propeller shaft angular velocity and D is the propeller diameter. Since the inflow velocity of the propeller affects the thrust output, the K_T is a function of the advance ratio J defined below

$$J = \frac{2\pi u_a}{\omega D} \tag{11}$$

where u_a is the inflow velocity of the propeller. From Eq. (10) it is clear that the advance ratio does not enter the definition directly. Blanke et al. (2000) showed that linear lift theory for propeller blades lead to the thrust

$$\tau_p = T_{|\omega|\omega}|\omega|\omega + T_{|\omega|u}|\omega|u_a \tag{12}$$

which in turn is equivalent to the approximation

$$K_T = \alpha_0 + \alpha_1 J \tag{13}$$

Access to the rotational velocity of the propeller is not always available, and hence a function to predict the rotational velocity based an input u e.g. *pulse-width-modulation* is necessary

$$\omega = f(u) \tag{14}$$

where $f(u)$ is a function of the input u to be defined later. In summary the problem is to identify the parameters $T_{|\omega|\omega}$ and $T_{|\omega|u}$ in Eq. (12) and the relevant elements of the damping matrix $\boldsymbol{D}$ and $\boldsymbol{M}$ from Eq. (7).

2.3. Multi-Vehicle Dynamics

Previous section described the model used for the individual subsystems in the construction of the larger model. This section presents the method employed to combine the subsystems into a unified multi-body system. This methodology was developed and presented in Nielsen et al. (2016a).

There exists multiple approaches to modelling of constrained multi-body systems. The modelling approaches can in general be partitioned into coordinate reduction or active constraint enforcement. A constraint can be seen as a restriction of the unconstrained system onto a manifold. Thereby coordinate reduction methods reduces the number of coordinates in the system until the description is only defined on the manifold itself. Conversely the active constraint enforcement methods allows the initial number of coordinates and instead projects the unconstrained motion onto the manifold at each iteration. Consequently the active constraint enforcement methods can deal with a variety of constraint types, whereas the coordinate reduction methods imposes more requirements on the constraint formulation. Furthermore the active constraint enforcement methods allows a more modular description to the combined system.

The approach chosen in this article belongs to the active constraint enforcement methods. The modelling formulation used for the unified systems is based on the Udwadia-Kalaba Formulation as presented in Udwadia and Kalaba (2002). The advantage of the Udwadia-Kalaba Formulation is that the projection onto the manifold is determined by use of the pseudo-inverse, hence, a solution can always be found even if the constraints are formulated in a redundant way. The cost, however, is the use of the Moore-Pensrose pseudo-inverse, which is often calculated using Singular-Value-Decomposition. In other words the computational requirements of the Udwadia-Kalaba method is higher than comparable methods, however, Laulusa and Bauchau (2008) noted that there exists methods to reduce the computational time required such as algorithms as full rank Cholesky factorization as was proposed in Courrieu (2008).

The individual vehicle system dynamics presented in Sec. 2.2 were performed in the local body-fixed frame. The derivation in body-fixed frame ensures the parameters of $\boldsymbol{D}$, $\boldsymbol{M}$ and $\boldsymbol{g}$ are time-invariant and furthermore that $\boldsymbol{M}$ does not become singular. The Udwadia-Kalaba Formulation was extended to *quasi-accelerations* and *quasi-velocities* in Udwadia and Phohomsiri (2007), which lays the foundation for the derivation in the following section. The quasi-coordinates are interchangeable with the body-fixed coordinates. Consider the transformation $\boldsymbol{J}(\boldsymbol{\eta}) \in \mathbb{R}^{n_\eta \times n_\nu}$ from Eq. (6) such that

$$\dot{\boldsymbol{\eta}} = \boldsymbol{J}(\boldsymbol{\eta})\,\boldsymbol{\nu} \tag{15}$$

where $\boldsymbol{\nu} \in \mathbb{R}^{n_\nu}$ is a vector of quasi-velocities while $\boldsymbol{\eta} \in \mathbb{R}^{n_\eta}$ and $\dot{\boldsymbol{\eta}}$ are generalised coordinates and generalised velocities respectively. An unconstrained Newtonian system can be described using quasi-coordinates mirroring that of Eq. (7).

$$\boldsymbol{M}\dot{\boldsymbol{\nu}}_u = \boldsymbol{S} \tag{16}$$

the subscript $(\cdot)_u$ symbolises the unconstrained quantities such that $\dot{\boldsymbol{\nu}}_u$ is the vector of unconstrained quasi-accelerations. Where $\boldsymbol{M} \in \mathbb{R}^{n_\nu \times n_\nu}$ is the inertia matrix and $\boldsymbol{S} \in \mathbb{R}^{n_\nu}$ is the generalised forces. It is important to notice that the model

is equivalent to the model of Eq. (7) for single vehicle systems. However, the model of Eq. (16) also applies for multi-vehicle systems with matrix $\boldsymbol{M}$ being block diagonal. The formulation in Eq. (16) can be transformed to a constrained formulation when exposed to constraints simply by augmenting with an additional term

$$\boldsymbol{M}\dot{\boldsymbol{\nu}}_c = \boldsymbol{S} + \boldsymbol{S}_c \tag{17}$$

where $\boldsymbol{S}_c \in \mathbb{R}^{n_\nu}$ is a vector of constraint forces. The challenge is then to calculate $\boldsymbol{S}_c$ such that both the system dynamics and the constraints are respected. Multiple different ways of obtaining the constraint forces exist and in this paper the Udwadia-Kalaba Formulation is chosen.

The solution to the constraint forces requires knowledge of the constraints themselves, and given n_c constraints the task is to put them on the following form

$$\boldsymbol{A}(\boldsymbol{\eta}, \boldsymbol{\nu})\,\dot{\boldsymbol{\nu}} = \boldsymbol{b}(\boldsymbol{\eta}, \boldsymbol{\nu}) \tag{18}$$

Notice from Eq. (18) that the constraint formulation requires the quasi-accelerations to be linear in the constraint matrix $\boldsymbol{A}$.

Generally the solution to the identification of constraint forces is reached by recasting the problem in a constrained optimisation framework. The Udwadia-Kalaba Formulation derives the constraint problem using Gauss' Principle of Least Constraint and reaches a solution based on the Moore-Penrose pseudo-inverse. Thereby, the constraint forces $\boldsymbol{S}_c$ can be identified by the equation below

$$\boldsymbol{S}_c = \boldsymbol{M}^{1/2}\left(\boldsymbol{A}\boldsymbol{M}^{-1/2}\right)^{+}\left(\boldsymbol{b} - \boldsymbol{A}\dot{\boldsymbol{\nu}}_u\right) \tag{19}$$

where the symbol $(\cdot)^{+}$ represents the Moore-Penrose pseudo-inverse. The constrained quasi-accelerations can then be identified by substituting into Eq. (17) and solving for $\dot{\boldsymbol{s}}_c$. Finally the constrained quasi-acceleration can then be identified by substituting Eq. (19) into Eq. (17) as shown below

$$\dot{\boldsymbol{\nu}}_c = \dot{\boldsymbol{\nu}}_u + \underbrace{\boldsymbol{M}^{-1/2}\left(\boldsymbol{A}\boldsymbol{M}^{-1/2}\right)^{+}\left(\boldsymbol{b} - \boldsymbol{A}\dot{\boldsymbol{\nu}}_u\right)}_{g(\dot{\boldsymbol{\nu}}_u,\, \boldsymbol{\nu}_c,\, \boldsymbol{\eta})} \tag{20}$$

Two observations can be made from Eq. (20). First, the constrained acceleration $\dot{\boldsymbol{\nu}}_c$ is the sum of the unconstrained acceleration $\dot{\boldsymbol{\nu}}_u$ and a constraining term that depends on the unconstrained acceleration. Secondly, it is clear that the Udwadia-Kalaba framework requires global knowledge of all states, which have implications when applied in a control context. The following section will define and derive the constraint necessary for describing the multi-body system.

2.4. The Rigid Constraint

The definition of the rigid constraint is given in Def. 2.1

Definition 2.1. *A rigid constraint is a constraint which restricts all relative motion between two rigid bodies.*

In essence the definition means that the two rigid bodies becomes one rigid body and the necessary number of constraints to formulate is all six relative DOFs. This section derives the generic formulation for a rigid constraint.

To allow for derivation of the constraint, two vehicles denoted $\{A\}$ and $\{B\}$ respectively, each with a local body-fixed frame attached are defined. Since the rigid constraints restrict all relative motion it is a purely geometric constraint. The constraint acts on both the relative distances, and on the relative orientations of the two bodies. The relative distance is maintained with respect to a mutual point s in the inertial frame. This formulation allows for the development of a loop-closure as shown in Fig. 1

The rotational constraint maintains a relative orientation between the vehicles. As the orientation is parametrised using quaternions, the relative orientation between them is the Hamilton product $\otimes$ between the quaternion of vehicle

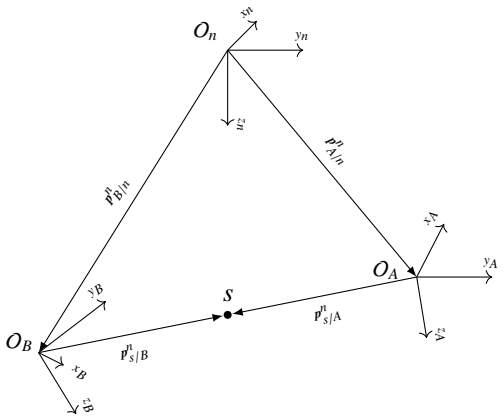

Figure 1: Constraint vector loop, O_n is the origin of the inertial space, O_i for $i \in \{A, B\}$ the origin of each vehicle. The point s is a common connection point between the vehicles.

A and the conjugate quaternion of vehicle B. The constraints are summarised as follows

$$\boldsymbol{c}_1 \ : \ \boldsymbol{p}^n_{A/n} + \boldsymbol{p}^n_{s/A} - \boldsymbol{p}^n_{B/n} - \boldsymbol{p}^n_{s/B} = 0 \tag{21}$$

$$\boldsymbol{c}_2 \ : \ \boldsymbol{q}^{(A)} \otimes \left(\boldsymbol{q}^{(B)}\right)^* = \tilde{\boldsymbol{q}} \tag{22}$$

where $\boldsymbol{q}^{(A)}$ is the unit quaternion of vehicle A, $\left(\boldsymbol{q}^{(B)}\right)^*$ is the quaternion conjugate of vehicle B and $\tilde{\boldsymbol{q}}$ is the relative rotation between vehicle A and B. As was shown in Sec. 2.3 the constraint formulation is required and enforced on acceleration level. In order to bring the constraints of Eq. (21) and (22) on the form of (18) a double time derivate is needed. Conducting the first time-differentiation on Eq. (21) and recalling that $\dot{\boldsymbol{R}}^n_b = \boldsymbol{S}(\boldsymbol{\omega}^n_{b/n})\boldsymbol{R}^n_b$ yields

$$\dot{\boldsymbol{p}}^n_{A/n} = \boldsymbol{R}^n_A \boldsymbol{v}^A_{A/n} \tag{23}$$

$$\dot{\boldsymbol{p}}^n_{s/A} = \boldsymbol{\omega}^n_{A/n} \times \boldsymbol{p}^n_{s/A} \tag{24}$$

Performing the first time derivative of the expressions (23) and (24) yields

$$\ddot{\boldsymbol{p}}^n_{A/n} = \boldsymbol{R}^n_A \dot{\boldsymbol{v}}^A_{A/n} + \boldsymbol{\omega}^n_{A/n} \times \boldsymbol{R}^n_A \boldsymbol{v}^A_{A/n}$$

$$\ddot{\boldsymbol{p}}^n_{s/A} = \dot{\boldsymbol{\omega}}^n_{A/n} \times \boldsymbol{p}^n_{s/A} + \boldsymbol{\omega}^n_{A/n} \times \left(\boldsymbol{\omega}^n_{A/n} \times \boldsymbol{p}^n_{s/A}\right)$$

For sake of space, the derivation is restricted to vehicle A, but it is noticed that the result is symmetric such that the derivation for vehicle B equals that of vehicle A with opposite signs. Adding together the expressions allows for the synthesis of the constraint matrix $\boldsymbol{A}$ for constraint $\boldsymbol{c}_1$

$$\boldsymbol{A}_1 = \begin{bmatrix} \boldsymbol{R}^n_A & -\boldsymbol{S}(\boldsymbol{p}^n_{s/A}) & -\boldsymbol{R}^n_B & \boldsymbol{S}(\boldsymbol{p}^n_{s/B}) \end{bmatrix} \tag{25}$$

The remainder of the expression is combined into the constraint vector $\boldsymbol{b}$

$$\begin{aligned} \boldsymbol{b}_1 = &-\boldsymbol{\omega}^n_{A/n} \times (\boldsymbol{R}^n_A \boldsymbol{v}^A_{A/n} + \boldsymbol{\omega}^n_{A/n} \times \boldsymbol{p}^n_{s/A}) \\ &+ \boldsymbol{\omega}^n_{B/n} \times (\boldsymbol{R}^n_B \boldsymbol{v}^B_{B/n} + \boldsymbol{\omega}^n_{B/n} \times \boldsymbol{p}^n_{s/B}) \end{aligned} \tag{26}$$

Moving to the orientation constraint $\boldsymbol{c}_2$ the Hamilton product between the unit quaternion of A and the conjugate of the unit quaternion of B yields the relative rotation between the vehicles. The time-differentiation of the attitude

constraint yields

$$\dot{\boldsymbol{q}}^{(A)} \otimes \left(\boldsymbol{q}^{(B)}\right)^* + \boldsymbol{q}^{(A)} \otimes \left(\dot{\boldsymbol{q}}^{(B)}\right)^* = \boldsymbol{0}$$

Conducting the second time derivative of the constraint along with a reduction yields

$$\ddot{\boldsymbol{q}}^{(A)} \otimes \left(\boldsymbol{q}^{(B)}\right)^* + \boldsymbol{q}^{(A)} \otimes \left(\ddot{\boldsymbol{q}}^{(B)}\right)^* + 2\left(\dot{\boldsymbol{q}}^{(A)} \otimes \left(\dot{\boldsymbol{q}}^{(B)}\right)^*\right) = \boldsymbol{0} \tag{27}$$

To express the resulting terms on the form in Eq. (18) a change of frame is necessary such that the quaternion change is on quasi-velocity form

$$\ddot{\boldsymbol{q}} = \boldsymbol{T}_q \dot{\boldsymbol{\omega}}^b_{b/n} + \dot{\boldsymbol{T}}_q \boldsymbol{\omega}^b_{b/n} \tag{28}$$

For convenience an additional matrix $\bar{\boldsymbol{H}}$ is defined as follows

$$\bar{\boldsymbol{H}}^{(i)} = \left[-\boldsymbol{\varepsilon}^{(i)} \quad \eta^{(i)}\boldsymbol{I}_3 + \boldsymbol{S}\left(\boldsymbol{\varepsilon}^{(i)}\right)\right] \text{ for } i \in \{A, B\} \tag{29}$$

notice the sign of the skew-symmetric matrix in $\bar{\boldsymbol{H}}$ has implications for the frame of rotation. $\boldsymbol{H}$ of Eq. (5) rotates the quaternion from global frame to the angular velocity of the local frame, while $\bar{\boldsymbol{H}}$ rotates from global frame to the angular velocity of the local frame relative to the global frame axes as shown below

$$\begin{aligned}\boldsymbol{\omega}^b_{b/n} &= 2\boldsymbol{H}\dot{\boldsymbol{q}} \\ \boldsymbol{\omega}^n_{b/n} &= 2\bar{\boldsymbol{H}}\dot{\boldsymbol{q}}\end{aligned}$$

The newly defined matrix allows for re-writing the relative rotation between two quaternions on linear form as follows

$$\begin{aligned}\boldsymbol{q}^{(A)} \otimes \left(\boldsymbol{q}^{(B)}\right)^* &= \begin{bmatrix} \left(\boldsymbol{q}^{(B)}\right)^T \\ \bar{\boldsymbol{H}}^{(B)} \end{bmatrix} \boldsymbol{q}^{(A)} = \boldsymbol{G}^{(B)}\boldsymbol{q}^{(A)} \\ &= \begin{bmatrix} \left(\boldsymbol{q}^{(A)}\right)^T \\ -\bar{\boldsymbol{H}}^{(A)} \end{bmatrix} \boldsymbol{q}^{(B)} = \boldsymbol{G}^{(A)}\boldsymbol{q}^{(B)}\end{aligned} \tag{30}$$

Applying the linear form to and combining the expressions in Eq. (27) and (28) yields

$$\begin{aligned}2\left(\dot{\boldsymbol{q}}^{(A)} \otimes \left(\dot{\boldsymbol{q}}^{(B)}\right)^*\right) &= 2\begin{bmatrix} \left(\boldsymbol{T}^{(B)}_q \boldsymbol{\omega}^B_{B/n}\right)^T \\ \dot{\bar{\boldsymbol{H}}}^{(B)} \end{bmatrix} \boldsymbol{T}^{(A)}_q \boldsymbol{\omega}^A_{A/n} \\ &= 2\dot{\boldsymbol{G}}^{(B)}\boldsymbol{T}^{(A)}_q \boldsymbol{\omega}^A_{A/n}\end{aligned} \tag{31}$$

The terms containing the double time derivative of the quaternions are brought on linear form to accommodate the requirement of Eq. (18)

$$\begin{aligned}\ddot{\boldsymbol{q}}^{(A)} \otimes \left(\boldsymbol{q}^{(B)}\right)^* &= \boldsymbol{G}^{(B)}\boldsymbol{T}^{(A)}_q \dot{\boldsymbol{\omega}}^A_{A/n} + \boldsymbol{G}^{(B)}\dot{\boldsymbol{T}}^{(A)}_q \boldsymbol{\omega}^A_{A/n} \\ \boldsymbol{q}^{(A)} \otimes \left(\ddot{\boldsymbol{q}}^{(B)}\right)^* &= \boldsymbol{G}^{(A)}\boldsymbol{T}^{(B)}_q \dot{\boldsymbol{\omega}}^B_{B/n} + \boldsymbol{G}^{(A)}\dot{\boldsymbol{T}}^{(B)}_q \boldsymbol{\omega}^B_{B/n}\end{aligned}$$

Finally the matrix and vector $\boldsymbol{A}_2$ and $\boldsymbol{b}_2$ associated with the constraints of $\boldsymbol{c}_2$ can be written as

$$\boldsymbol{A}_2 = \begin{bmatrix}\boldsymbol{0}_{4\times3} & \boldsymbol{G}^{(B)}\boldsymbol{T}^{(A)}_q & \boldsymbol{0}_{4\times3} & \boldsymbol{G}^{(A)}\boldsymbol{T}^{(B)}_q\end{bmatrix} \tag{32}$$

$$\boldsymbol{b}_2 = -\boldsymbol{G}^{(A)}\dot{\boldsymbol{T}}^{(B)}_q \boldsymbol{\omega}^B_{B/n} - \left(\boldsymbol{G}^{(B)}\dot{\boldsymbol{T}}^{(A)}_q + 2\dot{\boldsymbol{G}}^{(B)}\boldsymbol{T}^{(A)}_q\right)\boldsymbol{\omega}^A_{A/n} \tag{33}$$

Matrices $\boldsymbol{A}_1$ and $\boldsymbol{A}_2$ and vectors $\boldsymbol{b}_1$ and $\boldsymbol{b}_2$ are required for each rigid connection in the system.

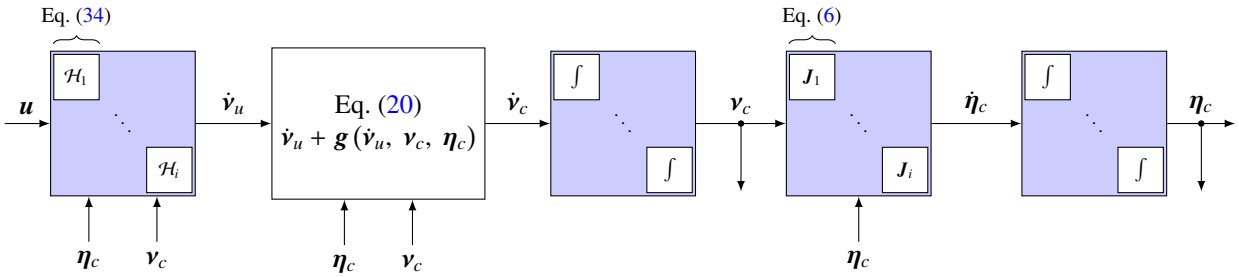

Figure 2: Block diagram of the simulation setup. The input vector $\boldsymbol{u}$ containing the thruster PWM signals is fed to the system in Eq. (34), which calculate the unconstrained accelerations $\dot{\nu}_u$. The unconstrained accelerations is then used in the Udwadia-Kalaba Formulation to produce the constrained accelerations $\dot{\nu}_c$.

2.5. Development of Simulator

The goal of the paper is to assess the applicability of multi-body dynamics for underwater systems. Up to now the focus has been on the individual models making up the total system. A simulator is needed to evaluate and compare the behaviour of the multi-body system. As discussed in Section 2.3 the modelling method is based on compensation and hence a complete state vector is kept for all vehicles. The vectors containing all the states of the system is defined as follows

$$\begin{aligned} \dot{\nu}_u &= [\dot{\nu}_u^{(1)}, \ldots, \dot{\nu}_u^{(i)}] \quad \dot{\nu}_c = [\dot{\nu}_c^{(1)}, \ldots, \dot{\nu}_c^{(i)}] \\ \nu_c &= [\dot{\nu}_c^{(1)}, \ldots, \dot{\nu}_c^{(i)}] \quad \dot{\eta}_c = [\dot{\eta}_c^{(1)}, \ldots, \dot{\eta}_c^{(i)}] \\ \boldsymbol{u} &= [\boldsymbol{u}^{(1)}, \ldots, \boldsymbol{u}^{(i)}] \end{aligned}$$

where $\boldsymbol{u}^{(i)}$ is the input vector containing the PWM signals for vehicle i, $\dot{\nu}_u^{(i)}$ is the vector of unconstrained acceleration of vehicle i, $\dot{\nu}_c^{(i)}$ is the vector of constrained acceleration of vehicle i. The vehicle subsystems are build from the dynamic model of Eq. (7), along with the propeller thrust model in Eq. (9), (8), (12) and (14). For clarity the vehicle subsystem is denoted $\mathcal{H}_i$ with i being the vehicle and defined as follows

$$\mathcal{H}_i : \begin{cases} \omega_j^{(i)} = f_j^{(i)}(u_j^{(i)}) & \text{Eq. (14)} \\ \tau_j^{(i)} = T_{|\omega|\omega}|\omega_j^{(i)}|\omega_j^{(i)} + T_{|\omega|u}|\omega_j^{(i)}|u_a^{(i)} & \text{Eq. (12)} \\ \boldsymbol{\tau}_{j/i}^{i} = \boldsymbol{t}_j^{i}\tau_j^{(i)} & \text{Eq. (8)} \\ \boldsymbol{\tau}^{(i)} = \sum_{j \in \mathcal{J}_i} \boldsymbol{h}\left(\boldsymbol{\tau}_{j/i}^{i}, \boldsymbol{p}_{j/i}^{i}\right) & \text{Eq. (9)} \\ \boldsymbol{M}^{(i)}\dot{\boldsymbol{\nu}}_u^{(i)} + \boldsymbol{D}^{(i)}(\boldsymbol{\nu}_c^{(i)})\boldsymbol{\nu}_c^{(i)} + \boldsymbol{C}^{(i)}(\boldsymbol{\nu}_c^{(i)})\boldsymbol{\nu}_c^{(i)} + \boldsymbol{g}^{(i)}(\boldsymbol{\eta}_c^{(i)}) = \boldsymbol{\tau}^{(i)} & \text{Eq. (7)} \end{cases} \tag{34}$$

where $\mathcal{J}_i$ is the set of thrusters mounted on the ith vehicle model, $u_j^{(i)}$ is the jth element of the ith vehicles input vector. Fig. 2 shows a block diagram of the simulator. First, each vehicle receives an input vector $\boldsymbol{u}$, the constrained state vector $\boldsymbol{\eta}_c$ and the constrained velocity vector $\boldsymbol{\nu}$, which is then simulated without constraints to obtain the unconstrained accelerations $\dot{\nu}_u$. Secondly, the Udwadia-Kalaba is invoked to calculate the constrained accelerations $\dot{\nu}_c$, which is then integrated to obtain the constrained body-velocities $\boldsymbol{\nu}_c$. Thereafter, the body-velocities are transformed using the kinematic transformation to obtain the constrained state derivates $\dot{\boldsymbol{\eta}}_c$. Finally, the new constrained state vector $\boldsymbol{\eta}_c$ is obtained through another integration.

3. Experimental Validation

This section describes the experimental set-ups employed for the investigation of the applicability of multi-body dynamics for underwater systems.

3.1. Lab Facilities and Equipment

All the experiments were conducted in the Marine Cybernetics Laboratories (MCLAB) located at Marinetek, NTNU, Trondheim, Norway. MCLab is a small wave basin measuring 40 by 6.45 m with a maximum depth of 1.5 m.

MCLAB features a towing carriage equipped with a Planar-Motion-Mechanism (PMM) and a high accuracy real-time underwater camera motion capture system, QUALISYS[1]. A detailed list of equipment in MCLab is available at the official homepage[2].

3.1.1. Single Vehicle, the BlueROV

The vehicle used in the investigation is the BlueROV from Bluerobotics[3]. The mass of the BlueROV is approximately 7.31 kg and it is capable of actuating all degrees of freedom.

The ROV is equipped with a Pixhawk autopilot running a forked version of the ArduSub software. The actuation of the vehicle is performed by six T200 thrusters also from BlueRobotics. The Pixhawk handles control of the thrusters through PWM signals send to the *Electronic-Speed-Controllers* (ESC) and provide different low-level controllers such as depth-hold, attitude-hold and other. The onboard computer in the BlueROV is an Odroid-XU4, which packs an ARM quad-core ARM-A15 and an ARM quad-core A-7 processor running Ubuntu 16.04 and Robot-Operating-System (ROS). The communication between the Pixhawk and the Odroid-XU4 is done through the MAVLink protocol on a UART connection using MAVROS.

A series of towing tank tests were conducted to identify the parameters of both hull and thrusters for the BlueROV. The BlueROV is attached to a bracket as shown on Fig. 3a and mounted on the towing carriage as shown on Fig. 3b. Three force measurement devices are used to measure the load of the vehicle; two are installed between the bracket and the towing carriage and one is attached on a thread between the ROV and the towing carriage.

A diagram of the system is shown on Fig. 4 where load cells m_1, m_2 are mounted between the bracket and carriage and strain gauge m_3 is attached by a wire at an angle ϕ. The angle ϕ was determined to be 47°. The ROV was mounted on the bracket and attached to the PMM of the towing carriage. Load cell m_3 is mounted at an angle ϕ hence the measured force includes a component not related to the motion of the vehicle. The total force acting on the bracket and vehicle is a function of all three measurements given in Eq. (35).

$$f_D = f_{m_1} + f_{m_2} - f_{m_3} \cos(\phi) \tag{35}$$

The sensors can only measure the total force applied to the bracket and therefore the identification of thruster and hull parameters is separated. The hull resistance is evaluated by first dragging the vehicle through water at different velocities to measure and then by conducting a polynomial fitting to the force measurements. The thruster performance is evaluated by dragging the vehicle through water at different velocities at different commanded thruster inputs. The load cells m_1 and m_2 were 18 kg load cells of the type PW2GC3 from Hottinger Baldwin Messtechnik GmbH (HBM)[4], while m_3 was a 5 kg strain gauge. At the time of the experiments the PMM was not able to conduct runs at constant acceleration and therefore the added mass could not be determined experimentally. Instead the added mass coefficients were identified based on calculations using WADAM and the CAD model of the vehicle.

3.1.2. Interconnected Multi-Vehicle System

Validation of the multi-body modelling methodology is conducted by applying different signals to the thruster of the vehicles and comparing the simulated trajectories to the measurements. This open-loop test strategy requires a mapping of all the inputs and outputs of the system. The inputs of the model is the thrust generated by the actuators

[1] Qualisys-Motion (2017)
[2] https://ntnu.edu/imt/lab/cybernetics
[3] Blue Robotics (2014)
[4] Hottinger Baldwin Messtechnik GmbH (HBM) (2017)

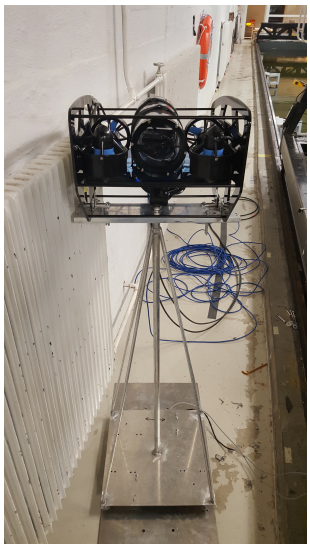

(a) BlueROV vehicle attached to the measurement bracket. The bracket is standing up side down on the side of the tank.

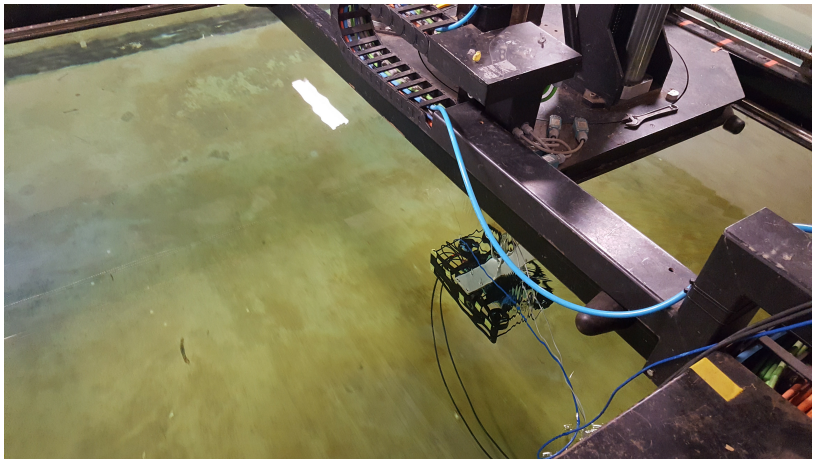

(b) Vehicle attached to bracket and mounted submerged underneath the towing carriage

Figure 3: The bracket with the vehicle attached mounted on the PMM in MCLAB

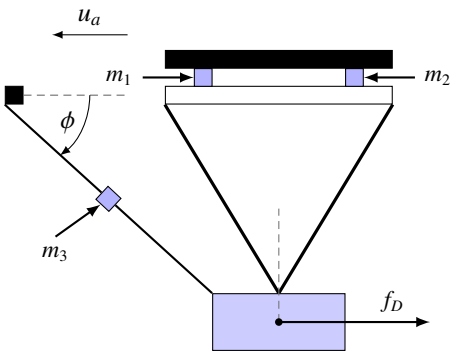

Figure 4: Diagram of the towing tank test setup with two load cells m_1 and m_2 attached between the towing carriage and bracket and a strain gauge m_3 attached though wire at an angle ϕ. The forward velocity u_a of the towing carriage and the induced drag force f_D are also shown.

and the water current, while the output is the measured position. Since MCLab is a controlled environment the current is known to be zero and the position of the vehicles is measured with high precision using the QUALISYS system. The interconnected system consists of two BlueROV vehicles joined together by a custom-made connection piece created from standard aluminium profiles. Fig. 5a shows the combined system of two BlueROVs joined by the connection piece.

The QUALISYS relies on two frames, a global frame O_n, and a body-fixed frame O_Q, which is positioned at a point Q on the moving system. The pose of the body-fixed frame denoted $\boldsymbol{\eta}_Q = [\boldsymbol{p}^n_{Q/n}, \boldsymbol{q}^{(Q)}]^T$ is then measured by QUALISYS. Fig. 5b shows the QUALISYS body-fixed O_Q, the global frame O_n and the position vector $\boldsymbol{p}^n_{Q/n}$ between the origins.

For brevity and without loss of generality only the body-fixed frame of the vehicle closest to the point Q is considered, and its body-fixed coordinate frame is denoted O_b. As the point Q does not intersect with origin of the body-fixed frame of the closest vehicle an additional lever-arm $\boldsymbol{p}^n_{Q/b}$ must be taken into account. The two body-fixed frames and the lever-arm can be seen on Fig. 5a.

The vehicle system was submerged and a series of motions were conducted by powering individual thrusters. The depth of the MCLAB tank imposed restriction of the possible motions of the vehicle system. To compensate for this restriction the experimental motions were limited to the horizontal plane. The horizontally directed thrusters were mounted off the $x-y$ gravity plane such that moments around the pitch and roll occurred during motion on the plane itself. Furthermore, the system was negatively buoyant, hence an active depth control was employed. A built-in depth and attitude controller was used to overcome the effects of the negative buoyancy and the thruster leverage arms and thereby isolate the motion to the horizontal plane.

3.2. Connector Parameters

The hydrodynamic parameters for the connection piece, which interconnects the two ROV systems (see Fig. 5a) were not identified experimentally. The connection piece is built up by square rods and therefore has a very simple geometry, which can easily be analysed with numerical procedures. The drag coefficients were found from steady state simulations using the CFD software Ansys Fluent 17.2. A realizable $K-\varepsilon$ turbulence model was used with a turbulence intensity of 5% at the inlet and outlet boundaries. A fine mesh with $2.3 \cdot 10^6$ elements were used to model the flow and an inflation layer of 6 elements were used to model the boundary layer. The added mass were found using the boundary element method program WADAM. Due to the simple geometry, the exact model was used in both the CFD and BEM analyses and the obtained coefficients should therefore be very accurate. The results from these analyses are shown in Table. 2.

Table 2: Dimensional hydrodynamic parameters of the connection piece

$X_{\dot{u}}$ $[kg]$	1.52	$X_{\lvert u\rvert u}$ $[\frac{kg}{m}]$	21.24
$Y_{\dot{v}}$ $[kg]$	0.52	$Y_{\lvert v\rvert v}$ $[\frac{kg}{m}]$	11.19
$Z_{\dot{w}}$ $[kg]$	1.50	$Z_{\lvert w\rvert w}$ $[\frac{kg}{m}]$	17.27
$K_{\dot{p}}$ $[kgm]$	0.021	$K_{\lvert p\rvert p}$ $[kgm]$	0.152
$M_{\dot{q}}$ $[kgm]$	0.01	$M_{\lvert q\rvert q}$ $[kgm]$	0.108
$N_{\dot{r}}$ $[kgm]$	0.025	$N_{\lvert r\rvert r}$ $[kgm]$	0.065

3.3. Multi-Vehicle Validation

A series of tests were performed. The horizontal plane was left uncontrolled and the surge directed thruster 1 and 2, where used in open-loop to generate the motion forward. The commanded PWM signals used where 1600 $[\mu s]$, 1700 $[\mu s]$ and 1800 $[\mu s]$. Due to the limited tracking space in the tank the thruster were only powered for 6 to 12 seconds depending on the experiment. The parameters collected were the commanded PWM values for all the thrusters in the system as well as the position and attitude of the QUALISYS frame.

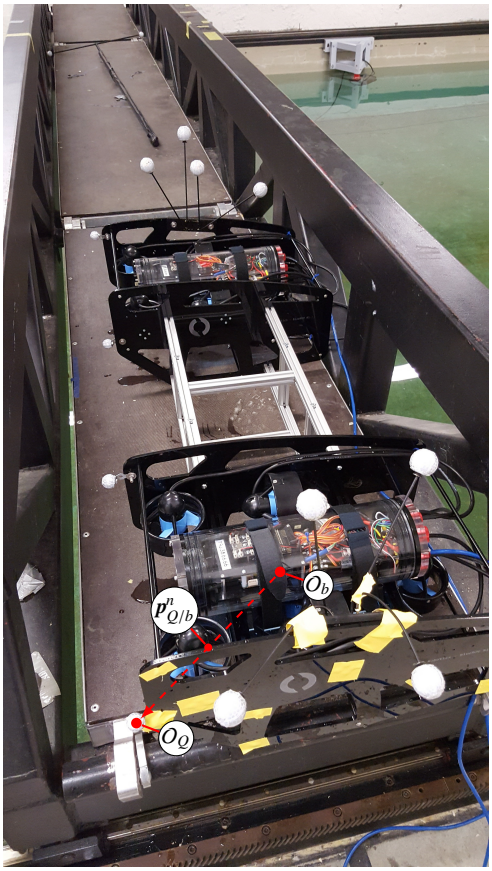

(a) Two BlueROV vehicles joined together by a connection piece made from aluminium profiles. The origin of the body-fixed QUALISYS frame O_Q and the origin of the vehicles body-fixed frame O_b are marked in red with the lever-arm vector $\boldsymbol{p}^n_{Q/b}$ shown.

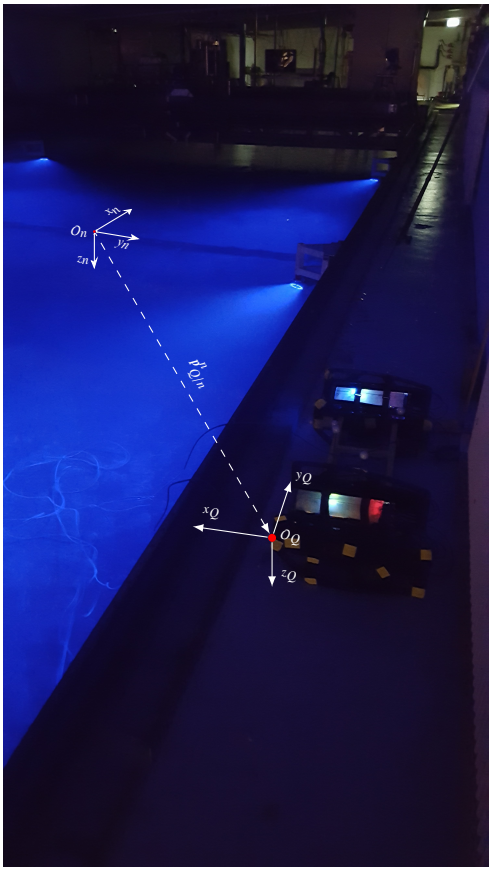

(b) The experimental setup with the active QUALISYS motion capture system in the background. The fixed and moving QUALISYS frames denoted O_n and O_Q respectively can be seen.

Figure 5: The interconnected ROV system used in the validation procedure for the multi-body modelling method.

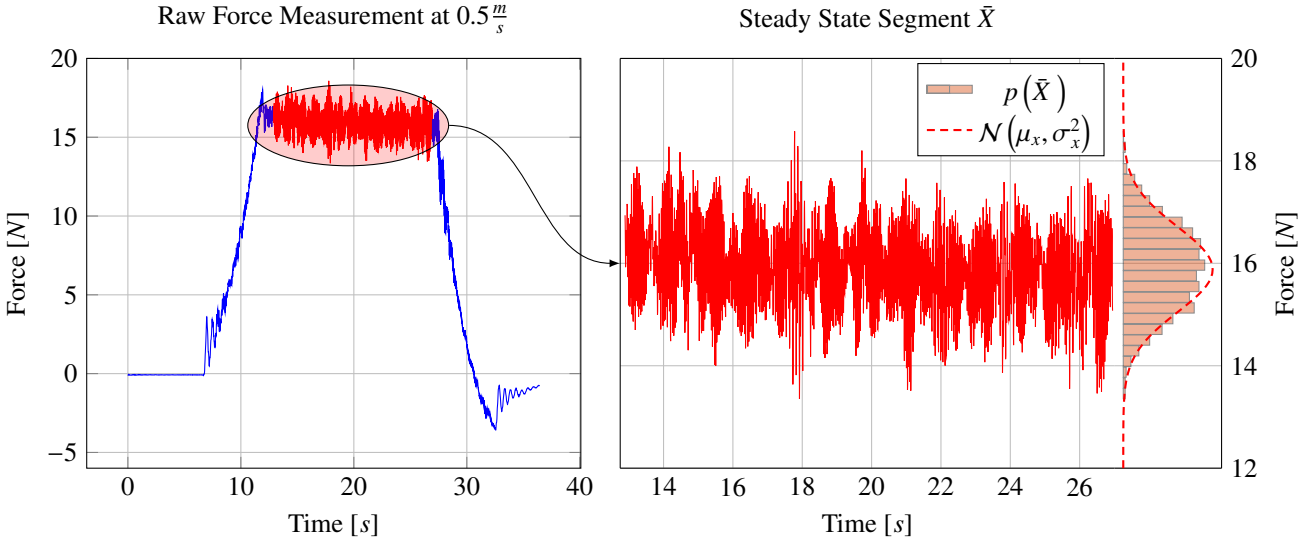

Figure 6: The steady state segment of each time series is extracted and reduced to a mean μ_x and a variance σ_x^2. The distribution of the signal around the steady state mean μ_x is close to a normal distribution

4. Results

This section presents the results of the two experimental trials conducted at MCLAB. In Sec. 4.1 the results of the towing tank tests are analysed and presented. Then in Sec. 4.2 the motion capture of the multi-body system from Sec. 3.3 is analysed based on the results obtained in Sec. 4.1.

4.1. Single Vehicle Parameter Identification

The trials were composed of multiple drag tests at multiple different velocities. Each run produced a time-series measurement dataset X from which a subset $\bar{X} \subset X$ contains a stationary part. The load cells and strain gauge are low cost devices and the signals are affected by significant amount of noise. To mitigate the noise each stationary subset was reduced to a statistic resulting in the expected value μ_x and the variance $P_x = \sigma_x^2$.

Fig. 6 shows an example time-series obtained from the surge drag estimation runs at $0.5\frac{m}{s}$. The left graph shows the whole dataset X with the stationary subset $\bar{X}$, and the right graph shows only the stationary part. The histogram shows the distribution of the signal segment with a normal distribution $\mathcal{N}\left(\mu_x, \sigma_x^2\right)$ for comparison. Multiple runs were conducted at each velocity to increase the statistical results.

The statistics of the runs were then fused using a weighted-least-squares (WLS) type algorithm to produce one point $\hat{x}$ for each velocity and an associated uncertainty P_x as shown below

$$P_x = \left(P_1^{-1} + \cdots + P_n^{-1}\right)^{-1} \tag{36}$$

$$\hat{x} = P_x\left(P_1^{-1}\mu_1 + \cdots + P_n^{-1}\mu_n\right) \tag{37}$$

The experiments are limited to allow for identification of uncoupled parameters. This limitation is consistent with Assumption 2.2. The hydrodynamic damping $\boldsymbol{D}(\boldsymbol{\nu})$ is a product of multiple components as discussed in Eidsvik and Schjølberg (2016a) and Fossen (2011). The effects of the different components can be collected into a linear an

quadratic term such that

$$f_D(u_a) = c_1|u_a|u_a + c_2 u_a \qquad (38)$$
$$c_1, c_2 \in \mathbb{R}_{\geq 0}$$

where c_1 and c_2 constitute the damping parameters.

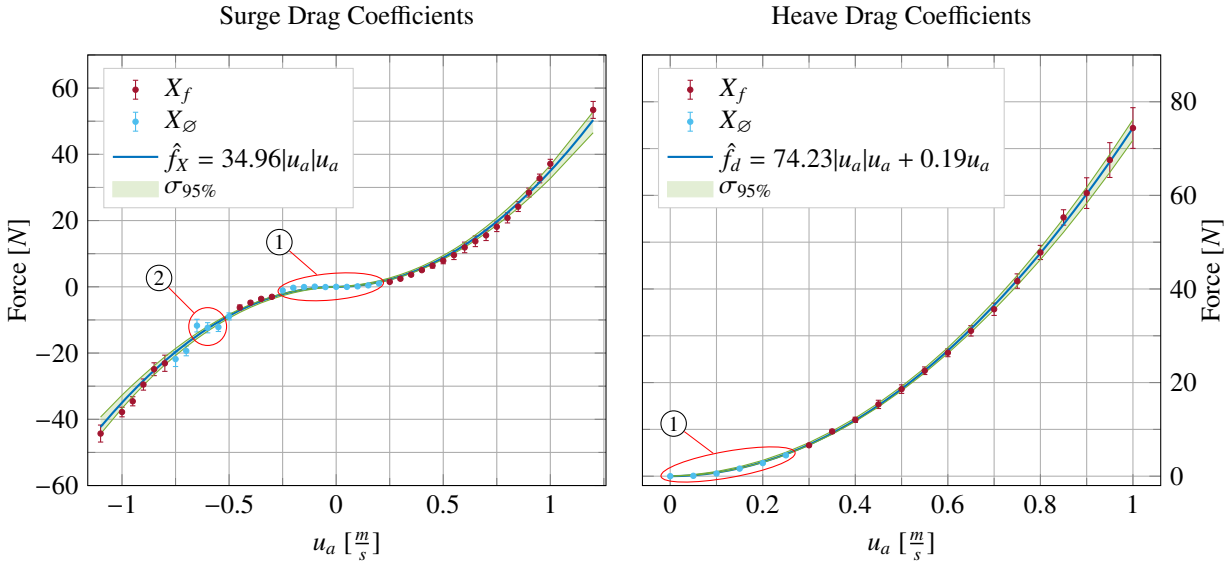

(a) Surge drag coefficient estimates for the single vehicle case with the fitting data X_f and excluded data $X_\varnothing$ along with the fitted curve and the associated 95% confidence interval. Two regions of data-points have been excluded. The points in (1) are removed due to lack of sensitivity of the sensors and points in (2) are excluded due to anomalies in the measurements.

(b) Heave drag coefficient estimates for the single vehicle case with the processed data X_f, the fitted curve $\hat{f}_X$ and the 95% confidence interval. In accordance with the results from the Surge fitting, the first data points highlighted by (1) are removed due to sensitivity. It is noted, however, that the disregarded points fit well with the polynomial estimate.

Figure 7: Towing tank tests results of the surge and heave direction for the single BlueROV vehicle

4.1.1. Translational Drag

The surge drag experiments consisted of 128 datasets with divided across 42 different velocities (21 forward and 21 backwards). Using Eq. (36) and (37) the 128 datasets were reduced to 41 data points. The 42 data points were partitioned into fitting data X_f and non-fitting data $X_\varnothing$. The data partitioning was motivated by observed abnormalities in the data as marked by (2) on Fig. 7a and the low sensitivity of the load cells at small amplitudes a significant amount of the data was excluded from the fitting marked by (1). The resulting data points of the fitting set X_f were used to fit Eq. (38) using bounded non-linear least squares.

Fig. 7a shows the resulting fitting along with confidence bounds.

The heave drag experiments were only performed in upwards direction and consisted of 61 datasets across 20 different velocities. As was the case with the surge drag, the points were reduced using the fusion formulas and divided into fitting data X_f and excluded data $X_\varnothing$. The resulting fitting is shown on Fig. 7b.

4.1.2. Rotational Drag

The rotational drag consisted of 25 datasets captured across 7 different velocities. The distribution of the noise was subject to additional dynamics which violated the assumption of normal distributed noise. Hence the fusion formulas

could not be used and instead the fitting points were picked by hand.

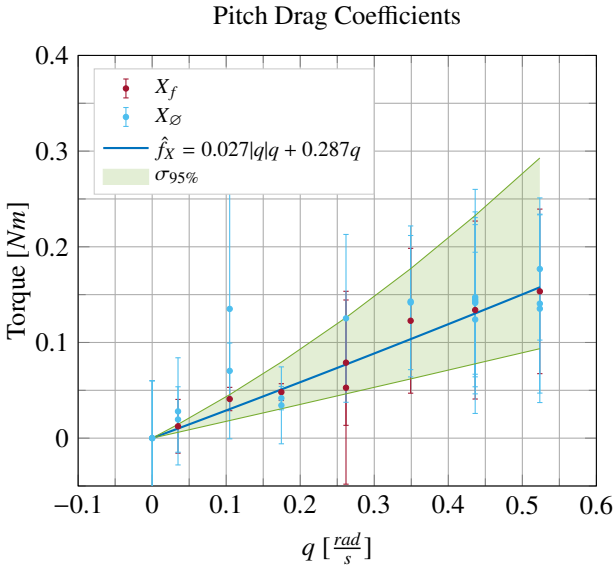

Figure 8: Pitch drag coefficient estimates for the BlueROV with the fitting data X_f and excluded data $X_\varnothing$ along with the fitted curve $\hat{f}_X$ and the associated 95% confidence interval. The fitting is dominated by the linear term, which is expected Caccia et al. (2000)

Fig. 8 shows that for small velocities the quadratic term in the drag torque vanishes. This is in accordance to the results obtained in Caccia et al. (2000).

4.1.3. Thruster Reduction

The flow conditions on the thrusters changes a function of the velocity through the water. Thereby, the thrust generated by the thrusters reduces as a function of the speed through water. The thrusters mounted on the BlueROV are the T-200 Thrusters also from BlueRobotics. They are controlled by the PixHawk through PWM signals to the ESCs. The rotational rate of the propeller thus depends on the load on the propeller. It was observed during the experiments and through the subsequent data analysis that the measured rotational rate of the propeller was not impacted by the water flow resulting from the motion of the vehicle. This implies no underlying dynamic relationship to consider and hence a static model for PWM to RPM can be done instead. The rotational rate was related to the PWM input through a fractional exponent relationship and the fitting is shown in Fig. 9.

$$f(x) = ax^{-b} + c \tag{39}$$

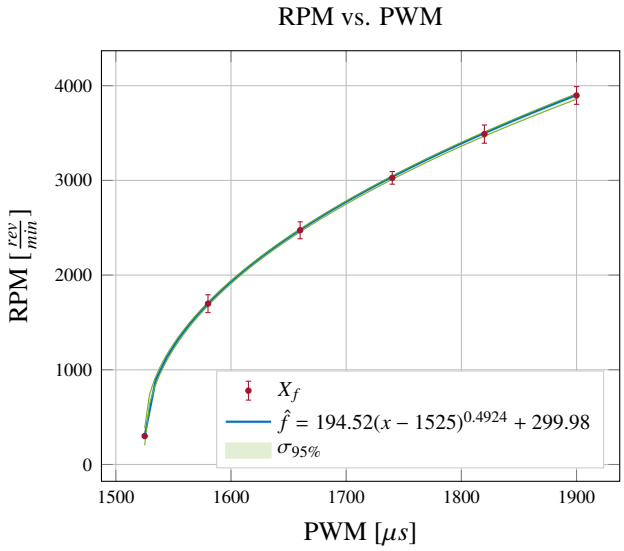

Figure 9: The RPM measurements are shown in X_f with 95% confidence bounds, the PWM to RPM fitting $\hat{f}$ is shown along with the 95% confidence interval. The estimated fitting intersects all the measurement points and the confidence of the parameters allows for a tight confidence interval.

There is variation present in the RPMs at each PWM instance, however, the variation is not correlated with the velocity through the water suggesting that the propeller load change was properly suppressed by the ESC.

The force measured under the experiments were compensated by the bracket and vehicle drag and in turn the the thrust coefficient K_T from Eq. (10) is calculated.

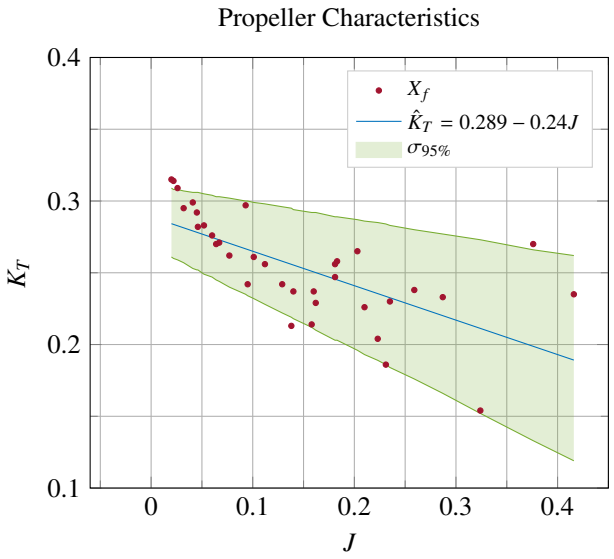

Figure 10: Dimensionless propeller characteristics data X_f and the linear estimate $\hat{K}_T$ versus the advance speed J

Fig. 10 shows the calculated thrust coefficients K_T from Eq. (10) and the linear estimate $\hat{K}_T$ from Eq. (13). Based on the thrust coefficient fitting shown in Fig. 10 the produced thrust of the propeller is reduced as velocity of the water across the propeller increases. This behaviour is consistent with the theory of Blanke et al. (2000). Evaluating the

thrust loss of each PWM at each velocity profile yields a map of thrust loss as shown in Fig. 11. Some inconsistencies are marked in the mapping. Specifically at $1740\mu s/0.7\frac{m}{s}$ marked by ① an increased propulsion is seen relative to the surrounding points. The same is true at $1820\mu s/0.8\frac{m}{s}$ marked by ② and subsequently all PWMs at $0.9\frac{m}{s}$ is either equal or increasing compared to at $0.8\frac{m}{s}$. It should be noted that the confidence intervals increase with the velocity. For velocities under $0.5\frac{m}{s}$ the thrust is consistently reduced across the operating range of the thruster. The overall

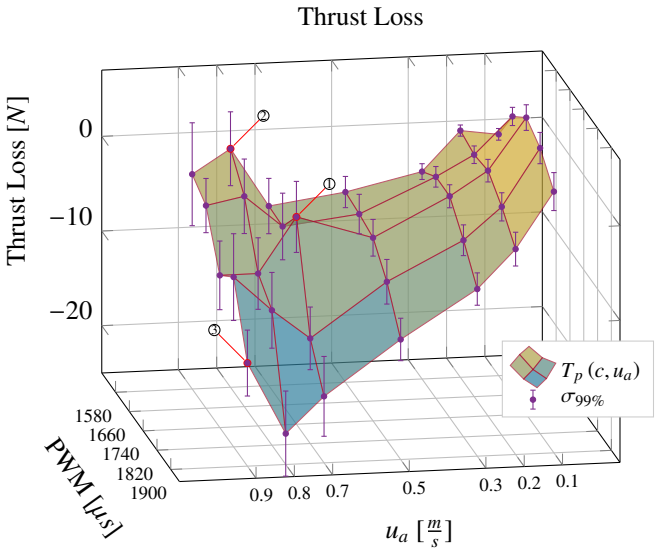

Figure 11: Thrust loss as function of PWM and forward velocity u_a with 99% confidence intervals at each point

result of the thruster mapping, however, is that the model of Eq. (12) is necessary to avoid overestimation of the produced thrust under motion.

4.1.4. Summary

In summary three DOFs, surge, heave and pitch were identified using towing tanks tests. The remaining three DOFs, sway, roll and yaw were not identified experimentally. As the remaining DOFs were necessary for the multi-body validation, they were extrapolated by using the ratio of the added mass coefficients.

$$K_{|p|p} = \left(\frac{K_{\dot{p}}}{M_{\dot{q}}}\right) M_{|q|q} \ , \ K_p = \left(\frac{K_{\dot{p}}}{M_{\dot{q}}}\right) M_q$$
$$N_{|r|r} = \left(\frac{N_{\dot{r}}}{M_{\dot{q}}}\right) M_{|q|q} \ , \ N_r = \left(\frac{N_{\dot{r}}}{M_{\dot{q}}}\right) M_q$$
$$Y_{|v|v} = \left(\frac{Y_{\dot{v}}}{Z_{\dot{w}}}\right) Z_{|w|w} \ , \ Y_v = \left(\frac{Y_{\dot{v}}}{Z_{\dot{w}}}\right) Z_w$$

Applying the equations to the experimentally acquired parameters yields estimates of the missing parameters. Table 3 shows an overview of the final values used in the subsequent simulations.

4.2. Multi-Vehicle Comparison

During the experiments the PWM input for each thruster was logged along with the measured pose from the Qualisys system. The comparison is conducted between simulations of the model driven by the PWM logged in the experiments from Section 3.1.2.

Table 3: Estimated dimensional hydrodynamic parameters for the BlueROV vehicle

$X_{\dot{u}}$ $[kg]$	2.6	$X_{\|u\|u}$ $[\frac{kg}{m}]$	34.96	X_u $[\frac{kg}{s}]$	0
$Y_{\dot{v}}$ $[kg]$	18.5	$Y_{\|v\|v}$ $[\frac{kg}{m}]$	103.25	Y_v $[\frac{kg}{s}]$	0.26
$Z_{\dot{w}}$ $[kg]$	13.3	$Z_{\|w\|w}$ $[\frac{kg}{m}]$	74.23	Z_w $[\frac{kg}{s}]$	0.19
$K_{\dot{p}}$ $[kgm]$	0.054	$K_{\|p\|p}$ $[kgm]$	0.084	K_p $[\frac{kgm}{s}]$	0.895
$M_{\dot{q}}$ $[kgm]$	0.0173	$M_{\|q\|q}$ $[kgm]$	0.028	M_q $[\frac{kgm}{s}]$	0.287
$N_{\dot{r}}$ $[kgm]$	0.28	$N_{\|r\|r}$ $[kgm]$	0.43	N_r $[\frac{kgm}{s}]$	4.64

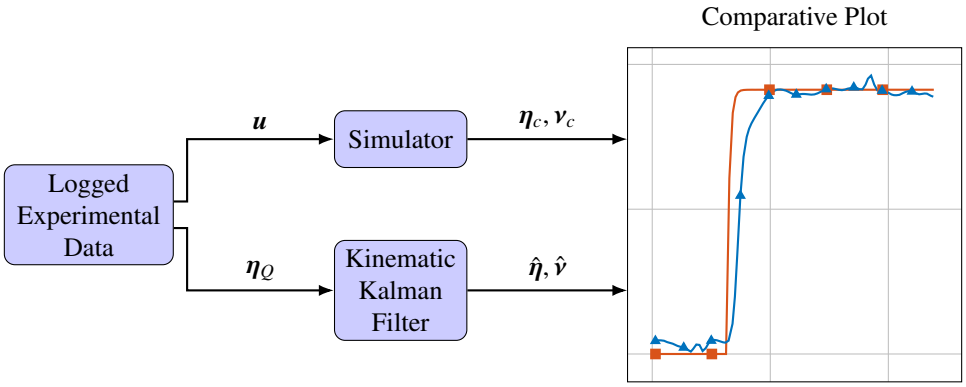

Figure 12: The figure shows the method of comparative study. First, the PWM signals logged in the experimental trails and the Qualisys pose vectors are fed to the simulator and Kinematic Kalman Filter respectively. Thereafter, the resulting pose and velocity vectors of the experimental data and simulation is compared.

The QUALISYS system measures only the pose of the attached coordinate frame, however, the actuation of the vehicles is applied on acceleration level. The difference in the type of measurement and input leaves a relative degree of 2 between the applied input and measured output. This means any error in the single vehicle parametric identification will aggravate twice through integrators. As the single vehicle model is based on approximation of polynomials, any results based on comparison of pose will produce questionable outcomes. To augment the analysis a kinematic Kalman Filter is employed to estimate the velocities based on the position data. Fig. 12 shows an overview of the comparison. The logged PWM inputs are used in the simulator described in Section 2.5 and the poses logged by the QUALISYS system are used in the correction step of the kinematic kalman filter to estimate the velocities. Thereafter, the resulting trajectories and velocities are compared.

Different motion patterns were performed to isolate the DOFs and thereby mitigate potential violations in the off-diagonal assumption 2.2.. The simplest isolated motion is a straight path, which is studied in Section 4.2.1. As the straight path motion contain no rotation another motion pattern, which focuses on exciting the rotational part of the system is investigated in Sec. 4.2.2.

4.2.1. Straight Path Trials

The straight path motion is the simplest conceivable motion possible. The motion isolates the surge DOF dynamics and thereby reduces potential uncertainty introduced by interaction with other DOFs.

As was described in Sec. 3.3 the restricted depth of the tank reduced the possible motions of the system to the horizontal plane. To enforce this restriction a built-in depth hold controller was used to maintain a height in the water column. As a consequence, all analyses are restricted to the X-Y axis of the global frame.

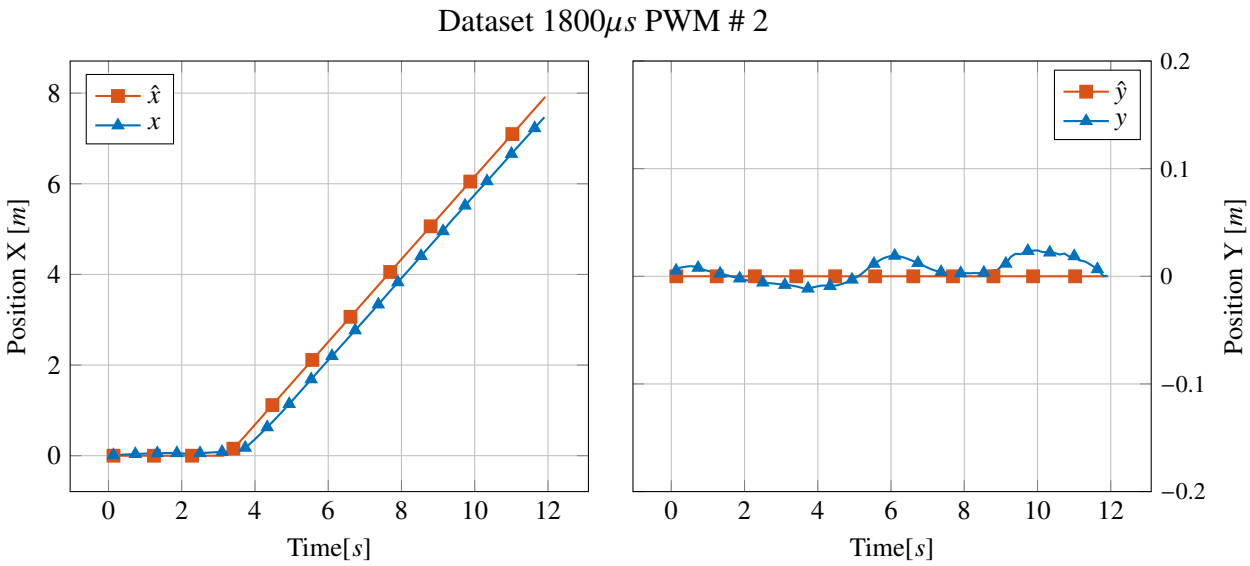

(a) comparison between the simulated forward position $\hat{x}$ and the measured forward position x

(b) Comparison between the simulated sideways position $\hat{y}$ and the measured sideways position y

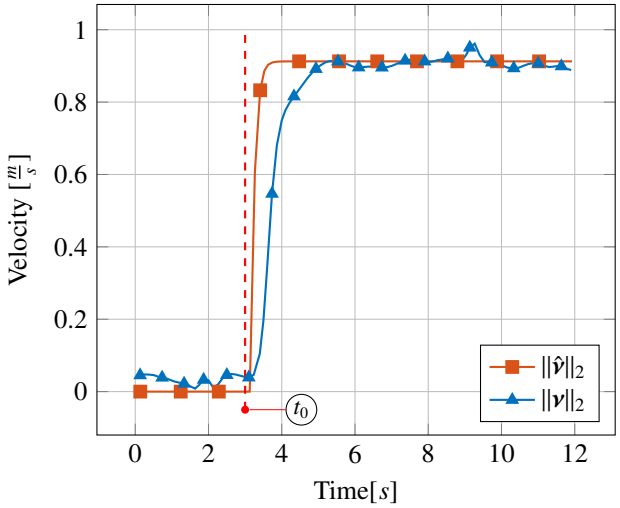

(c) Comparison of the simulated and measured velocity profiles denoted $||\hat{\nu}||_2$ and $||\nu||_2$ respectively. The time of thruster engagement is marked by (t_0) (- - -)

Figure 13: Time-series comparison of a straight run dataset in the horizontal plane. The dataset is the last captured set with 1800[μs] PWM on all surge thrusters.

A total number of 14 datasets were collected during the experimental trails. The length of each dataset spans 12 seconds, where the first 3 seconds are zero-input steady state conditions until surge thrusters were engaged. A time series comparison between the X and Y positions and the normed velocity $||\nu||_2$ of the last collected dataset and the simulation is shown on Fig. 13. Fig. 13a shows the position of the simulated and measured data along the forward x-axis. The profile is in agreement especially with respect to the gradient of the curve, however, there is a time delay between the measurements and simulation after the thrusters are engaged. The reason for the delay is most likely multifactorial. First the thrusters are assumed static, that is the propeller spin-up delay is neglected as it was assumed very small. Secondly the tether cables extruding from each of the vehicles are not modelled. The tether cables

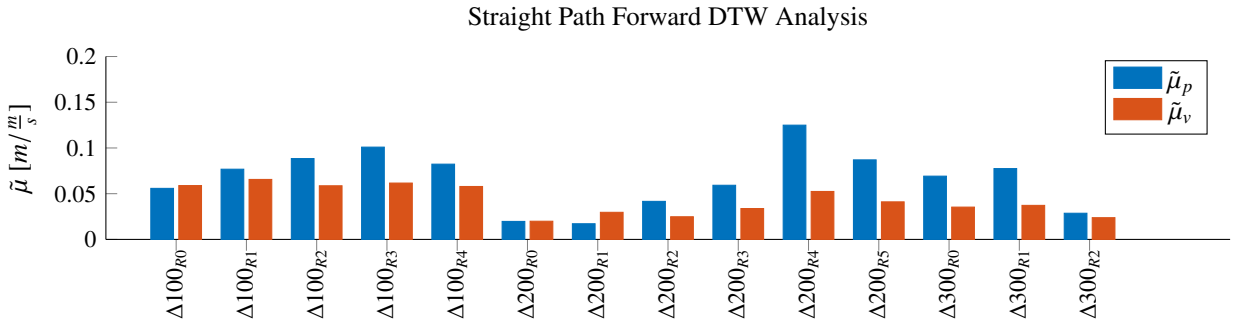

Figure 14: Average $\|\cdot\|_2$ error distance $\tilde{\mu}$ between the simulation and the positional data and velocity data respectively for the straight path trials. The x-axis shows the datasets named by their difference from the baseline 1500[μs]. The average error distance is low compared to the total distance travelled.

introduces additional rigid-body mass, hydrodynamic added mass and drag, which in turn decreases the acceleration and steady-state velocity of the combined system. Fig. 13c support this hypothesis. The comparison between the $\|\cdot\|_2$ of the horizontal velocity components from the simulation and measurements, shows that the rise-time of the simulation is smaller than that of the measurements while the difference in steady-state conditions are negligible suggesting that the cable drag is a non-significant factor. This makes sense since the cables were dragged after the vehicles thus remaining streamlined with respect to the direction of flow.

Using the drag coefficient of a flat plate in turbulent conditions the drag force of the cable can be estimated as

$$\begin{aligned} F_d &= \frac{1}{2}\rho D \phi C_t |u_a| u_a L \\ &\Downarrow \\ &= 0.12 |u_a| u_a L \end{aligned}$$

which is negligible for the relevant velocities and cable lengths.

The initial steady-state velocity error between the simulation and measurement in Fig. 13c is attributed to the depth and attitude hold controller. The attitude controllers of the vehicles were initially *Proportional-Integral-Derivative* (PID) type controllers, however, small differences in the estimated attitude in each vehicles induced build-up fluctuations of the integral part. Therefore the integral term of the controllers was removed at the cost of small steady-state errors in the attitudes.

The Qualisys and RC data is sampled at different rates. As the RC data is used to drive the simulation a direct comparison between the simulation and measurements is not possible. Furthermore as was shown on Fig. 13 the velocity and x position profiles were in agreement except for a time-delay. This time-delay has a profound impact on trajectory outcome of the simulation versus the data. A measure of similarity, which is robust with respect to time delay, is necessary to quantify the comparison between data and simulation. While technically not a metric the *Dynamic Time Warp* (DTW) is a commonly used measure of similarity between time series data. The DTW matches points between time series to minimize the metric distance between them. A DTW transformation of each dataset is conducted and the average euclidean distance between the position trajectory in x-y between the simulation and data and the velocity is calculated. Fig. 14 shows the results of the calculated averages for each dataset, where the x-axis signifies the increased PWM from baseline 1500[μs] denoted ΔPWM. Fig. 13 showed the data from $\Delta 300_{R2}$, which has an error of $0.027m$ and $0.025\frac{m}{s}$ respectively. Overall the average errors between the simulations and the measurements are upper bounded by $0.15m$ and $0.1\frac{m}{s}$ respectively.

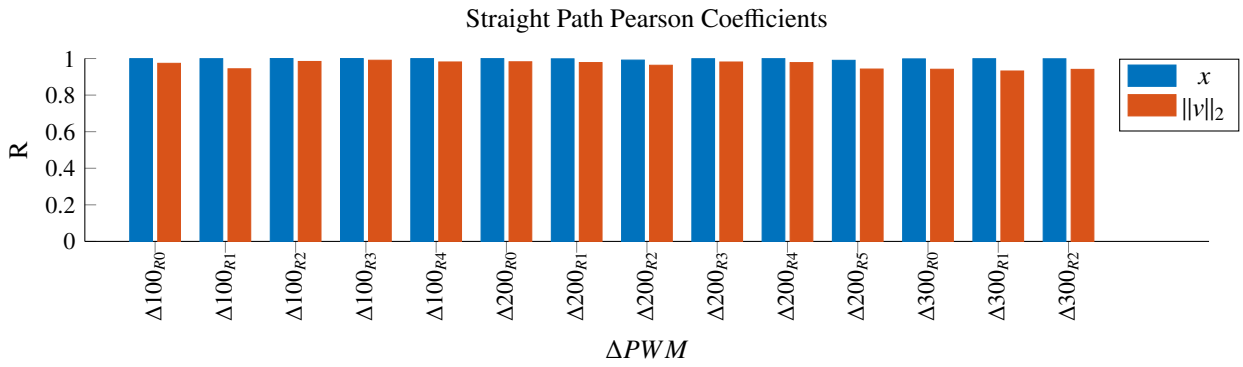

Figure 15: Pearson R coefficients for the forward position x and the 2-norm of the velocity vector $\|v\|_2$ for the straight path trails. The x-axis shows the dataset as the difference from the baseline 1500[μs].

4.2.2. Rotational Trails

The former section focused on translational motion without rotation. This section expands the analysis from non-rotational to rotational excitation in combination with translational motion.

The experiment was devised such that only the left ROV engaged its surge directed thrusters. The motion resulting from this differential thruster scheme was an initiation of a forward motion for the port side ROV, which in turn triggered a starboard turn from the drag of the right ROV. A series of runs were conducted and Fig. 16 shows an analysis of a single run. The horizontal position components are shown on Fig. 16a. The trajectory of the system forms a circle, which is evident as the x and y components each forms a sinusoidal curve. Qualitatively both the x and y curves of the simulation and data are in agreement, however, the is an offset in between the data and simulation. Furthermore, the peak-to-peak distance in both x and y for data and simulation respectively are equal, meaning the diameter of the resulting circular trajectory is equal for the simulation and measurements. Fig. 16b shows the heading angle for the simulation and measurements. Apart from a time-delay in the measurements the resulting curves are very similar. The heading is positively increasing, which is to be expected as thrust on only the port side will induce a starboard turn. Fig. 16c shows the euclidean norm of the horizontal velocity vector. As was the case before the steady-state velocity of the simulation matches exactly that of the measurements. The difference in rise-time, however, suggests that the mass parameters in the simulation is underestimated. This again can be explained by the extra mass from the wires. Furthermore, the velocity reduction in the end differs between the measurement and simulation with measurement dropping faster to $0\frac{m}{s}$ suggesting that the ratio between linear and quadratic damping may be wrong with the linear part being underestimated. Finally on Fig. 16d shows a comparison between the body angular velocity r and the simulated counterpart $\hat{r}$. The rise-time and transients of the angular velocity curves are very similar. This adds strength to the assumption that any inconsistencies in the translational velocity was from added wire mass as the effect on the rotational inertia should be minimal.

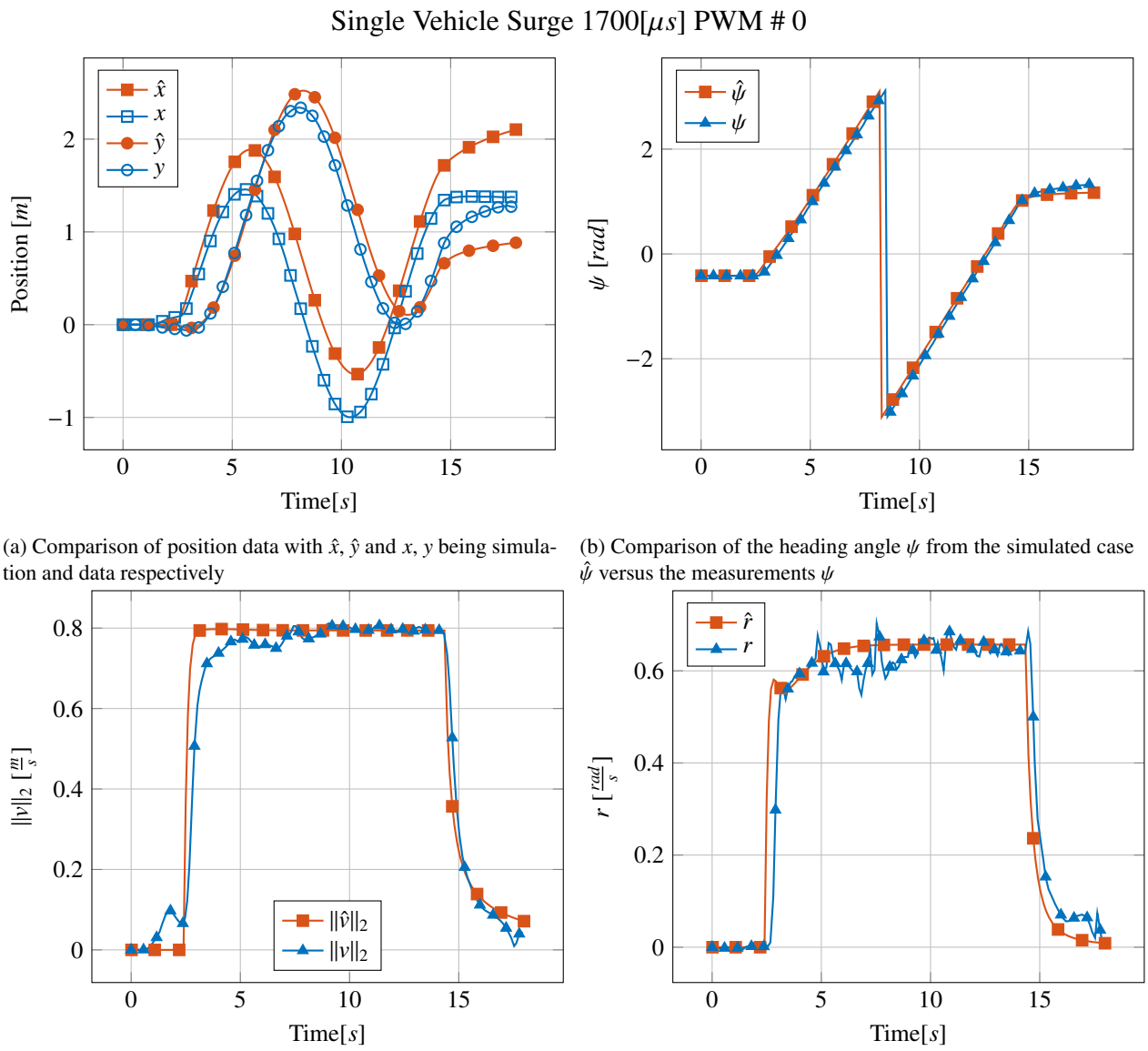

(a) Comparison of position data with $\hat{x}$, $\hat{y}$ and x, y being simulation and data respectively

(b) Comparison of the heading angle ψ from the simulated case $\hat{\psi}$ versus the measurements ψ

(c) Comparison of the euclidean $\|\cdot\|_2$ of the horizontal velocity components of the simulation $\|\hat{v}\|_2$ and the measurements $\|v\|_2$

(d) Comparison between the angular body velocity r extrapolated from measurements and the simulated counterpart $\hat{r}$

Figure 16: Analysis of single dataset from the rotational trials, where the left-most ROV is engaging surge thrusters at $\Delta 200 \mu s$ forward direction.

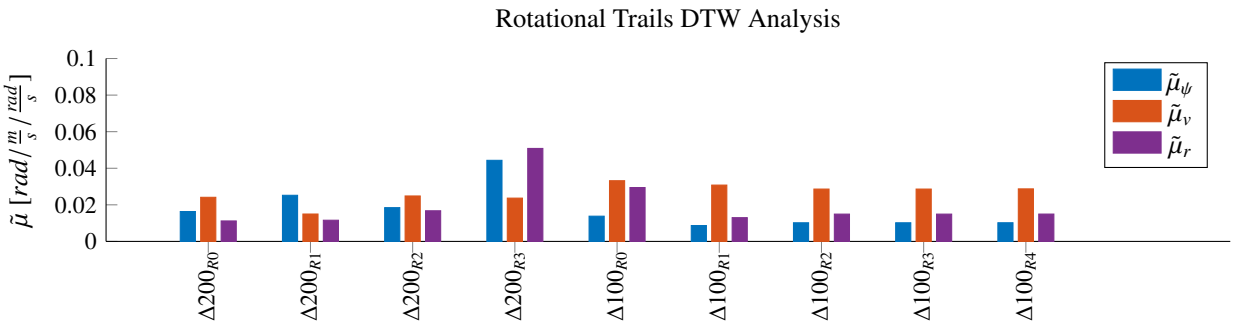

Figure 17: The average euclidean error between the simulated and measured heading angle ψ, velocity v and body angular velocity r with the x-axis showing the datasets as differences between the baseline 1500[μs]. The average error is very small suggesting a good agreement in the behaviour of the simulations versus the experimental data.

To represent all the results of the trajectories another DTW analysis is conducted. As DTW is not scale and rotational invariant, the position variables are not considered. Instead the average heading angle $\tilde{\mu}_\psi$, the 2-norm of the velocity vector $\tilde{\mu}_{\|v\|_2}$ and the body angular velocity $\tilde{\mu}_r$ is considered. The results are shown on Fig. 17. The errors between the simulations and measurements are very small.

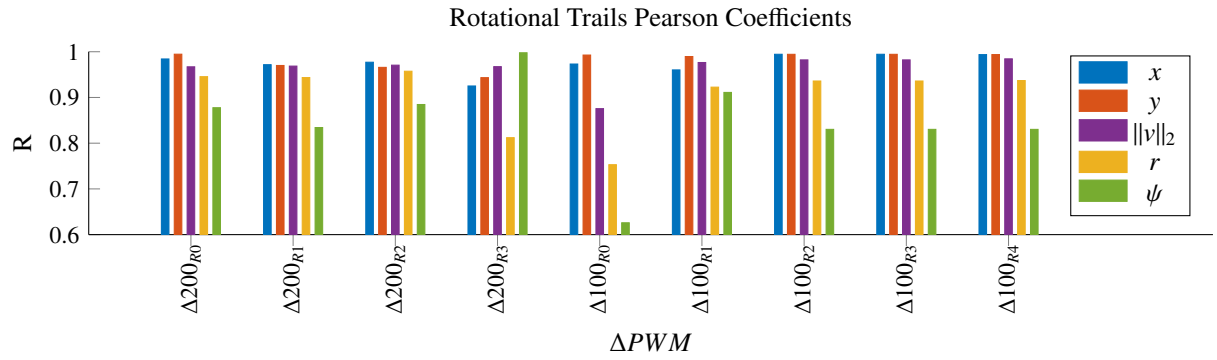

Figure 18: The Pearson R coefficients for x, y, $\|v\|_2$, r and ψ respectively for each of the datasets at different ΔPWM. The correlation between the simulation and experimental data is very high.

Another common tool for comparison of curves is the *Pearson R Correlation*. In Fig. 18 the Pearson R coefficient is shown for a number of different variables. Generally the correlation between the curves are very high except for $\Delta 100_{R0}$.

5. Discussion

In this paper two types of experiments have been performed to verify the methodology for developing systems dynamics and parameter identification of an interconnected multi-vehicle system. The syste mwas run in along a straight path trajectory and rotational trajectory. The comparison was conducted on both velocity and position to attenuate possible errors in the identified coefficients. The results of the comparison between the simulations and the measurements showed that an overall good agreement. The rise-time of the velocity was lower in the simulated case, which was likely due to the missing mass of the umbilical cables. The steady-state velocity was very similar both in translational and rotational motion, which suggested that proximity effects induced by hull to hull interaction was negligible.

6. Conclusion

Motivated by the large potential for future sub-sea use of multiple collaborating and interconnected underwater vehicles, this paper focused on development of a methodology for automated modelling of interconnected underwater robots. The paper suggested a systematic approach that utilize a model of a single underwater vehicle and constraints derived from the topology of interconnected vehicles, to obtain a mathematical model of the a cluster of modular underwater robots.

The modelling methodology was based on the Udwadia-Kalaba formulation for constrained dynamics and was shown to allow for a modular description of re-configurable underwater robots. The paper showed that the suggested formulation forms a very convenient and generic framework to model interconnected underwater vehicles. Experimental verification was shown on a specific instance of a modular system consisting of two vehicles. Evaluation of the accuracy of the model showed that the most significant dynamics was indeed captured by the resulting model.

The approach is believed to be an important step towards automated control-redesign for a cluster of modular robots that autonomously could change their configuration, thereby bringing us closer to implementation of underwater autonomous modular systems, a technology that is envisaged to become instrumental for inspection and condition assessment when more and more equipment is placed as stationary installations on the sea-bed.

Future work will focus on using the newly modelling method to develop closed loop controllers for coupled vehicles.

Acknowledgement

This work has been carried out at the Centre for Autonomous Marine Operations and Systems (AMOS), supported by the Research Council of Norway through the Centres of Excellence funding scheme, project number 223254 — AMOS. The Norwegian research Council is acknowledged as the main sponsor of AMOS.

The authors gratefully acknowledge the colleagues at Technical University of Denmark, Department of Automation and Control, Roberto Galeazzi and Adriana Gabriela Zsuzsan for providing access to BlueROV hardware and for support before and during the experimental tests. The same should go to Frederik Jelshøj Hansen for design and manufacturing of the connection element. Furthermore gratitude is given to the Glenn Angell at the Department of Engineering Cybernetics for expedite preparation of necessary components for the experimental setup.

References

Allotta, B., Conti, R., Costanzi, R., Giardi, F., Meli, E., Ridolfi, A., 2013. Modelling and control of an autonomous underwater vehicle for mobile manipulation. Proceedings of the ECCOMAS Thematic Conference on Multibody Dynamics 2013.

Antonelli, G., 2014. Underwater Robots. Vol. 2 of Springer Tracts in Advanced Robotics. Springer Berlin Heidelberg, Berlin, Heidelberg.

Avila, J. J., Nishimoto, K., Mueller Sampaio, C., Adamowski, J. C., 2012. Experimental investigation of the hydrodynamic coefficients of a remotely operated vehicle using a planar motion mechanism. Journal of Offshore Mechanics and Arctic Engineering 134 (2), 021601.

Avila, J. P. J., Adamowski, J. C., 2011. Experimental evaluation of the hydrodynamic coefficients of a rov through morison's equation. Ocean Engineering 38 (17-18), 2162–2170.

Blanke, M., Lindegaard, K., Fossen, T., 2000. Dynamic model for thrust generation of marine propellers. Manoeuvring and Control of Marine Craft 2000 (MCMC2000): 5th IFAC Conference on Manoeuvring and Control of Marine Craft.

Blue Robotics, August 2014. Website, online; accessed 14 June 2017.
URL http://www.bluerobotics.com/

Caccia, M., Indiveri, G., Veruggio, G., apr 2000. Modeling and identification of open-frame variable configuration unmanned underwater vehicles. IEEE Journal of Oceanic Engineering 25 (2), 227–240.

Casalino, G., Caccia, M., Caiti, A., Antonelli, G., Indiveri, G., Melchiorri, C., Caselli, S., 2014. Maris: A national project on marine robotics for interventions. 2014 22nd Mediterranean Conference on Control and Automation, MED 2014, 864–869.

Conti, R., Meli, E., Ridolfi, a., Allotta, B., 2015. An innovative decentralized strategy for i-auvs cooperative manipulation tasks. Robotics and Autonomous Systems 72, 261–276.

Courrieu, P., 2008. Fast computation of moore-penrose inverse matrices. Neural Information Processing - Letters and Reviews 8 (2), 25–29.

Eidsvik, O. A., Schjølberg, I., 2016a. Determination of hydrodynamic parameters for remotely operated vehicles. In: Proceedings of the ASME 2016 35th International Conference on Ocean, Offshore and Arctic Engineering. ASME, Busan, pp. 1–10.

Eidsvik, O. A., Schjølberg, I., 2016b. Time domain modeling of rov umbilical using beam equations. IFAC-PapersOnLine 49 (23), 452–457.

Eng, Y., Lau, W., Low, E., Seet, G., Chin, C., 2008. Identification of the hydrodynamics coefficients of an underwater vehicle using free decay pendulum motion. Engineering Letters 16 (3), 326–331.
Ferri, G., Manzi, A., Fornai, F., Ciuchi, F., Laschi, C., 2013. A systematic method for dynamic modeling and identification of a small-sized autonomous surface vehicle using simulated annealing techniques. 2013 MTS/IEEE Oceans - Bergen.
Fossen, T. I., 2011. Handbook of Marine Craft Hydrodynamics and Motion Control, 1st Edition. Wiley and son, Trondheim.
Gomes, S., Zanela, E., Pereira, A., 2016. Automatic generation of dynamic models of cables. Ocean Engineering 121, 559–571.
Hottinger Baldwin Messtechnik GmbH (HBM) , 2017. Website, online; accessed 14 June 2017.
URL http://www.hbm.com/
Huang, H., Tang, Q., Li, H., Liang, L., Li, W., Pang, Y., sep 2016. Vehicle-manipulator system dynamic modeling and control for underwater autonomous manipulation. Multibody System Dynamics, 1–23.
Huston, R. L., Kamman, J. W., 1982. Validation of finite segment cable models. Computers & Structures 15 (6), 653–660.
Kamman, Huston, 2001. Multibody dynamics modeling of variable length cable systems. Multibody System Dynamics 5 (3), 211–221.
Kamman, J. W., Huston, R. L., 1985. Modelling of submerged cable dynamics. Computers and Structures 20 (1-3), 623–629.
Kelasidi, E., Liljebäck, P., Pettersen, K. Y., Gravdahl, J. T., dec 2015. Experimental investigation of efficient locomotion of underwater snake robots for lateral undulation and eel-like motion patterns. Robotics and Biomimetics 2 (1), 8.
Kelasidi, E., Pettersen, K. Y., Gravdahl, J. T., dec 2014a. A control-oriented model of underwater snake robots. In: 2014 IEEE International Conference on Robotics and Biomimetics (ROBIO 2014). IEEE, pp. 753–760.
Kelasidi, E., Pettersen, K. Y., Gravdahl, J. T., sep 2014b. Modeling of underwater snake robots moving in a vertical plane in 3d. In: 2014 IEEE/RSJ International Conference on Intelligent Robots and Systems. IEEE, pp. 266–273.
Kim, J., Kim, K., Choi, H. S., Seong, W., Lee, K. Y., 2002. Estimation of hydrodynamic coefficients for an auv using nonlinear observers. IEEE Journal of Oceanic Engineering 27 (4), 830–840.
Krishnamurthy, P., Khorrami, F., De Leeuw, J., Porter, M. E., Livingston, K., Long, J. H., 2009. A multi-body approach for 6dof modeling of biomimetic autonomous underwater vehicles with simulation and experimental results. Proceedings of the IEEE International Conference on Control Applications, 1282–1287.
Laulusa, A., Bauchau, O. A., 2008. Review of classical approaches for constraint enforcement in multibody systems. Journal of Computational and Nonlinear Dynamics 3 (1), 011004.
Marco, D., Martins, A., Healy, A., 1998. Surge motion parameter identification for the nps phoenix auv. In: 1st Int. Workshop on Autonomous Underwater Vehicles for Shallow Water and Coastal Environment. IARP, Lafayette, IN, pp. 197–210.
Moe, S., Antonelli, G., Pettersen, K. Y., 2014. Null-space-based behavior guidance of planar dual-arm uvms. 2014 IEEE International Conference on Robotics and Biomimetics, IEEE ROBIO 2014, 735–740.
Nielsen, M. C., Blanke, M., Schjølberg, I., 2016a. Efficient modelling methodology for reconfigurable underwater robots. IFAC-PapersOnLine 49 (23), 74–80.
Nielsen, M. C., Blanke, M., Schjølberg, I., 2016b. Experimental validation of dynamic multi-body modelling for reconfigurable underwater robots. Oceans 2016 MTS/IEEE, 6.
Palomeras, N., Peñalver, A., Massot-Campos, M., Negre, P., Fernández, J., Ridao, P., Sanz, P., Oliver-Codina, G., oct 2016. I-auv docking and panel intervention at sea. Sensors 16 (10), 1673.
Park, J., Kim, N., 2015. Dynamics modeling of a semi-submersible autonomous underwater vehicle with a towfish towed by a cable. International Journal of Naval Architecture and Ocean Engineering 7 (2), 409–425.
Pereira, J., Duncan, A., 2000. System identification of underwater vehicles. Proceedings of the 2000 International Symposium on Underwater Technology, UT 2000, 419–424.
Qualisys-Motion, 2017. Website, online; accessed 14 June 2017.
URL http://www.qualisys.com/
Ramírez-Macías, J. A., Brongers, P., Rúa, S., Vásquez, R. E., 2016. Hydrodynamic modelling for the remotely operated vehicle visor3 using cfd. IFAC-PapersOnLine 49 (23), 187–192.
Ridao, P., Tiano, A., El-Fakdi, A., Carreras, M., Zirilli, A., dec 2004. On the identification of non-linear models of unmanned underwater vehicles. Control Engineering Practice 12 (12 SPEC. ISS.), 1483–1499.
Ross, A., Fossen, T. I., Johansen, T. A., 2004. Identification of underwater vehicle hydrodynamic coefficients using free decay tests. In: IFAC Conference on Control Applications in Marine Systems. pp. 363–368.
Santhakumar, M., 2013. Investigation into the dynamics and control of an underwater vehicle-manipulator system. Modelling and Simulation in Engineering 2013, 1–13.
Sanz, P. J., Ridao, P., Oliver, G., Melchiorri, C., Casalino, G., Silvestre, C., Petillot, Y., Turetta, A., 2010. TRIDENT: A framework for autonomous underwater intervention missions with dexterous manipulation capabilities. Vol. 7. IFAC.
Schjølberg, I., Gjersvik, T. B., Transeth, A. A., Utne, I. B., 2016. Next generation subsea inspection, maintenance and repair operations. IFAC-PapersOnLine 49 (23), 434–439.
Tarn, T. J., Shoults, G. a., Yang, S. P., 1996. A dynamic model of an underwater vehicle with a robotic manipulator using kane's method. Autonomous Robots 3 (2-3), 269–283.
Udwadia, F. E., Kalaba, R. E., 2002. On the foundations of analytical dynamics. International Journal of Non-Linear Mechanics 37, 1079–1090.
Udwadia, F. E., Phohomsiri, P., jun 2007. Explicit poincaré equations of motion for general constrained systems. part i. analytical results. Proceedings of the Royal Society A: Mathematical, Physical and Engineering Sciences 463 (2082), 1421–1434.
Valeriano-Medina, Y., Martínez, A., Hernández, L., Sahli, H., Rodríguez, Y., Cañizares, J., 2012. Dynamic model for an autonomous underwater vehicle based on experimental data. Mathematical and Computer Modelling of Dynamical Systems 3954 (July), 1–26.
Yang, K., 2016. Dynamic model and cpg network generation of the underwater self-reconfigurable robot. Advanced Robotics 1864 (May), 1–13.